Mineralium Deposita (2019) 54:1033–1052
https://doi.org/10.1007/s00126-018-0858-5

ARTICLE

Structural controls on granitoid-hosted gold mineralization and paleostress history of the Edikan gold deposits, Kumasi Basin, southwestern Ghana

Ghislain Tourigny[1] · Markos D. Tranos[2] · Quentin Masurel[3] · Oliver Kreuzer[4,5] · Steffen Brammer[1] · Kwaku Owusu-Ansah[6] · David Yao[1] · Thomas Hayford[7]

Received: 25 June 2018 / Accepted: 20 November 2018 / Published online: 18 December 2018

Abstract

The > 9 Moz total aggregate gold endowment at the Edikan mine, Kumasi Basin, Ghana, is contained within a cluster of orogenic gold deposits located along the Akropong fault zone. The granitoid-hosted orebodies at Edikan (e.g., AG2, AG3, Fobinso, Esuajah), essentially an interconnected mesh of gold-bearing quartz veins, formed during deformation event D_{3Edk}, which postdates the penetrative regional D_{2Edk} deformation. The gold-bearing quartz veins developed in, and adjacent to, N-S- and NW-SE-trending, low-angle thrust faults that crosscut lithological contacts and earlier formed, steeply dipping D_{2Edk} faults. Our paleostress analysis shows that the D_{3Edk} deformation, during which the mineralized fault system developed, was characterized by a WNW-ESE "hybrid" compression that evolved to a strike-slip regime. This progressive deformation is best described with the following stress regimes: WNW-ESE transpression-pure compression (T1) associated with low-angle thrusting, subsequent transpression-strike-slip (T2), and later strike-slip-transtension (T3) associated with steeply dipping strike-slip faulting. The bulk of the granitoid-hosted gold mineralization at Edikan is associated with two principal sets of gold-bearing quartz veins, including low-angle fault-fill veins controlled by thrusts and shallow dipping oblique-extension veins that developed during T1. The activation of the reverse and sinistral strike-slip faults led to the development of restraining jogs characterized by abundant shallow and steeply dipping gold-quartz veins with moderately NE-plunging ore shoots. The geometry of the mineralized fault-fracture meshes is consistent with fault-valve behavior in a horizontal compressive stress regime under sustained conditions of supralithostatic fluid pressures at low differential stress.

Keywords Fault-fill vein · Extension vein · Orogenic faulting · Orogenic gold · Kumasi Basin · Ghana

Editorial handling: H. Frimmel

✉ Ghislain Tourigny
ghislain.tourigny@perseusmining.com

[1] Perseus Mining Côte d'Ivoire, Cocody 2 Plateaux vallon, quartier Lemania 28 BP 571, Abidjan, Côte d'Ivoire

[2] Department of Geology, Aristotle University of Thessaloniki, 54124 Thessaloniki, Greece

[3] Centre for Exploration Targeting, The University of Western Australia, 35 Stirling Highway, Crawley, WA 6009, Australia

[4] Corporate Geoscience Group, PO Box 5128, Rockingham Beach, WA 6969, Australia

[5] Economic Geology Research Centre, James Cook University, Townsville, QLD 4811, Australia

[6] SEMS Exploration, P.O. Box 2805, Osu, Accra, Ghana

[7] Perseus Mining Ghana, Chancery Court, 147A Giffard Road, East Cantonments, Accra, Ghana

Introduction

Granitoid-hosted gold deposits represent an economically significant style of gold mineralization in the Birimian granite-greenstone belts of southern Ghana (Fig. 1). Examples include the Subika and Chirano gold deposits in the Sefwi Belt (e.g., Allibone et al. 2004; Baah-Danso 2011); the Nhyiaso, Ayankyerim, and Edikan gold deposits in the eastern Kumasi Basin (e.g., Fougerouse et al. 2017); and the Dynamite Hill and Abore gold deposits along the Asankragwa shear zone in the central Kumasi Basin (e.g., Chudasama et al. 2016). In Ghana, granitoid-hosted gold deposits are commonly centered upon small granitic plugs and/or narrow dikes. The latter are typically only mineralized over relatively short strike lengths (up to km scale) with economic gold grades restricted to specific dilational and restraining structural settings. The relatively limited spatial extent of granitoid-hosted ore shoots compared to the overall

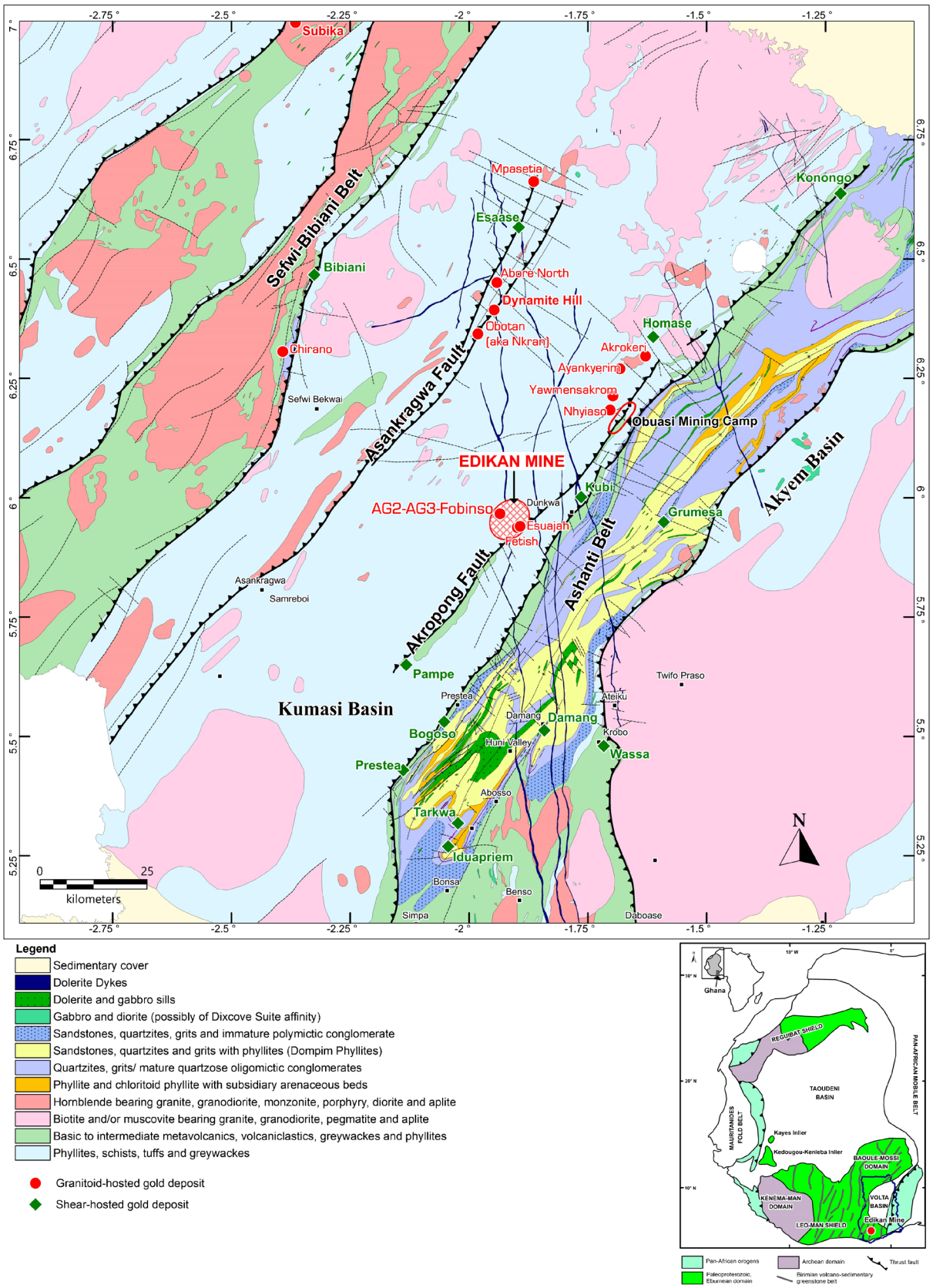

Fig. 1 Simplified geological map showing the location of the Edikan gold mine and granite-hosted gold deposits in southwestern Ghana (modified after Perrouty et al. 2012)

size of the host intrusions implies a strong structural control centered upon specific parts of the host intrusions. However, little detailed information is available about what processes and features may have interacted to localize gold mineralization in these settings.

In an attempt to improve our knowledge of the controls on the geometry of granitoid-hosted gold deposits at Edikan, we undertook detailed mapping of the AG2-AG3-Fobinso open pits. The AG2-AG3-Fobinso deposits are hosted in a continuous, up to 160 m wide and greater 4.7 km long, NE-SW-striking granodiorite dike and conjointly host a resource of about 2.3 Moz Au at an average grade of 1.1 g/t Au.

This paper documents the structural controls of granitoid-hosted gold mineralization at the scale of the AG2-AG3-Fobinso deposits and aims to better constrain the brittle deformation recorded by these deposits by providing a detailed paleostress history and evolution of the gold-bearing structures.

Regional setting

The Edikan gold mine in southwestern Ghana is situated within the Kumasi Basin (cf. Adadey et al. 2009) of the Leo-Man Shield, a tectonostratigraphic element of the West African Craton (Jessell et al. 2016). Structurally, Edikan is located along the first-order Akropong fault zone near the western flank of the Ashanti granite-greenstone belt (Fig. 1). The Akropong fault zone, which is subparallel to the NE-SW-trending Ashanti Belt and steeply NW-dipping, has been interpreted as an early basin growth fault that was later reactivated as a reverse fault (Perrouty et al. 2012). In addition to Edikan, the Akropong fault zone also controlled the location of the Pampe gold deposit (e.g., Salvi et al. 2016) to the southwest, whereas the giant Obuasi gold deposit (> 60 Moz) to the northeast of Edikan is located at the intersection between the Akropong fault zone and the lithospheric-scale Ashanti fault system (Duodu et al. 2009; Perrouty et al. 2012).

The metasedimentary successions of the Kumasi Basin were intruded by distinct generations of granitoids (Fig. 1), most of which were emplaced during the Eburnean orogeny between ca. 2115 and 2080 Ma (e.g., Oberthür et al. 1998; Parra-Avila et al. 2015). The long axes of these granitoids are generally subparallel to the penetrative NE-SW-striking structural grain recorded by the metasedimentary country rocks. Granitoids at the Edikan mine are similar in composition and relative and absolute timing to the so-called basin-type intrusive bodies that occur along the western flank of the Ashanti belt (e.g., Anyankyerim, Nhyiaso, Yaomensakrom, and Ayanfuri: Yao and Robb 2000). These intrusions have crystallization ages of 2105 ± 2 Ma (Oberthür et al. 1998). For comparison, the Esuajah North granite at Edikan was dated at 2105 ± 3 Ma (Oberthür et al. 1998).

The structural evolution of southwestern Ghana was polyphase: an early phase of crustal thickening was followed by one of strike-slip (transcurrent) tectonics marked by a progression in deformation style from ductile to brittle behavior (Feybesse et al. 2006). The polyphase structural evolution reported from selected gold deposits in the Kumasi Basin is presented in Table 1. The structural history of the nearby Obuasi gold deposit is used as a reference frame in this study of the granitoid-hosted AG2-AG3-Fobinso gold deposits at the Edikan gold mine.

Gold mineralization in southwest Ghana occurred over a protracted interval between 2100 to 2065 Ma and was temporally associated with a minor transcurrent deformation event during the waning stages of, or following, regional-scale contractional deformation (Allibone et al. 2002; Pigeois et al. 2003; Duodu et al. 2009; Perrouty et al. 2012).

Geology of the AG2-AG3-Fobinso open pits, Edikan mine

The Edikan mine area (Fig. 2) covers several granitoid- and shear zone-hosted gold deposits. This study focused on the AG2-AG3-Fobinso gold deposits (Fig. 3) where detailed open pit and field mapping have been carried out at 1:1000 scale (contemporaneous with ongoing mining activities) and the field data have been corroborated with geological and structural information from oriented diamond drill holes.

Three principal rock types have been recorded at Edikan: (i) metasedimentary country rocks, (ii) barren and locally gold-bearing granodiorite dikes and plugs, and (iii) late cross-cutting quartz and feldspar phyric granite dikes (Figs. 2 and 3). These rocks are well exposed in the open pits up to a vertical depth of approximately 160 m. The metasedimentary rocks mainly comprise metasandstone, graphitic shale, and carbonaceous phyllite. They belong to the Kumasi Group, a sequence of sedimentary rocks distributed throughout the Kumasi Basin and metamorphosed to greenschist facies (muscovite-chlorite) during regional metamorphism ascribed to the Eburnean orogeny (Chudasama et al. 2016). The metasandstone has a fine- to medium-grained texture and is composed mainly of detrital quartz, shale fragments, and clasts of mafic volcanic rocks, chlorite, white mica and albite with calcite-ankerite, ilmenite, and pyrite as accessory minerals. The graphitic shale and phyllite are composed mainly of quartz, mica, pyrite, and graphite.

As illustrated in Figs. 2 and 3, the metasedimentary country rocks were intruded by dikes and small irregular plugs of granodiorite. The dikes are undeformed but contain xenoliths of strained country rock (i.e., foliated metasedimentary rocks) indicating that their emplacement postdates development of the penetrative regional foliation. Plug-like granodiorite intrusions, such as at Esuhaja North, Esuhaja South, Fetish, and

Table 1 Deformation history and relative timing of gold mineralization at Edikan and nearby gold deposits

Obuasi gold deposit (~ 60 Moz)	Edikan gold camp (~ 9 Moz)	Asankrangwa gold camp (~ 10 Moz)	Pampe gold deposit (~ 0.5 Moz)
D1Ob early convergence: Bedding-parallel shearing and rarely preserved S1	D1Edk early convergence: Bedding-parallel shearing and rarely preserved S1 in hinge zones to F2 W-striking recumbent folds F1		
D2Ob NW-SE-directed compression: Steeply dipping NE-striking penetrative S2, F2 tight to isoclinal folding; NE-striking thrusts and high-angle reverse faults Large quartz shear veins Subhorizontal stretching (L2) and boudinage Greenschist facies metamorphism *First-stage mineralization in Fougerouse et al. 2017: disseminated gold-bearing sulfides (Apy, Py)	D2Edk NW-SE-directed compression: Steeply dipping NNE- to NE-striking penetrative S2, F2 tight to isoclinal folding NE-trending high-angle reverse shear zones Late-kinematic granitoid emplacement Greenschist facies metamorphism	D1Ask-D2Ask progressive NW-SE to WNW-ESE shortening: Steeply dipping NE-striking S1 Steeply dipping NNE-striking S2, F1-F2 tight to isoclinal folding, NE-striking thrusts and high-angle reverse faults Greenschist facies metamorphism	D1Pa NW-SE-directed compression: Steeply dipping NE-striking penetrative S1, F1 tight to isoclinal folding, NE-striking thrusts and high-angle reverse faults
D3Ob NNW-SSE-directed shortening (local?): Gently dipping E- to ENE-striking S3 Asymmetrical NE- to ENE-striking F3 folds Folding of the Ashanti fault *Second-stage mineralization in Fougerouse et al. 2017: high-grade visible gold in deformed quartz veins (Au, Gn, Ccp, Sp, Brn…)		D3Ask NE-SW-directed shortening (local?): Steeply dipping NW- to WNW-trending domainal crenulation cleavage S3 Open to tight moderately to steeply plunging NW-striking F3 folds	D2Pa WSW-ENE-directed shortening (local?): Steep NNW-striking crenulation cleavage S2
D4Ob NNW-SSE-directed shortening: Reactivation of D2Ob structural architecture; N-striking sinistral strike-slip faults Asymmetric dilatant breccias	D3Edk, WNW-ESE- to NW-SE-directed shortening: Low-angle thrusts in granitic dike Shallow dipping extension vein arrays in granite dike Reactivation of D2Edk structural architecture, oblique sinistral-reverse displacement	D4Ask NNW-SSE-directed shortening: Sinistral strike-slip reactivation of D1Ask-D2Ask structural architecture, oblique sinistral-reverse displacement *Gold mineralization: shear-hosted and fault meshes in granitoid, sulfides (Apy, Py) within fault zones and wall rocks sediments	D3Pa NNW-SSE-directed shortening: Reactivation of D1Pa structural architecture Steep ENE-striking crenulation cleavage S3 Steep conjugate vein sets (strike-slip)
*Single-stage mineralization in Oberthür et al. 1998 and Allibone et al. 2002: shear-hosted gold	*Vein-hosted gold mineralization		*Vein-hosted gold mineralization
References: Blenkinsop et al. 1994; Oberthür et al. 1998; Allibone et al. 2002; Fougerouse et al. 2017	This study	References: Chudasama et al. 2016; Gelber 2018	Reference: Salvi et al. 2016

Chirawewa, are broadly similar to the dikes with respect to mineralogy and texture (Fig. 2).

A number of quartz-feldspar porphyry dikes of granitic composition cut both the metasedimentary rocks and the granodiorite (Fig. 3). These dikes are subvertical and strike NE-SW to ESE, have an average thickness of about 5 m, and are barren and undeformed. Many of these dikes can be traced for more than 100 m along strike and are known to extend to a depth of at least 150 m (Fig. 3).

A few subvertical, NNW-SSE-striking dolerite dikes have been mapped based on aeromagnetic data. These dikes cross-cut the sedimentary country rocks and regional tectonic fabric (Fig. 2). The dolerite dikes are considered part of a large Mesozoic dike swarm cutting across SW Ghana with dike emplacement linked to brittle, ridge-parallel deformation at the time of the breaking away of the African continent from South America (Jessell et al. 2015). According to new U-Pb age data, the NNW-SSE dolerite dikes are ca. 867 million years old (Baratoux et al. in press).

The dominant structural features at Edikan and in the AG2-AG3-Fobinso open pits consist of mainly NE-SW-trending and steeply NW-dipping brittle-ductile faults that are defined by narrow domains of quartz-sericite-carbonate and graphitic schist. Among these major regional structures are the Bokitsi Fault, Akropong Fault, and unnamed subsidiary faults along lithological contacts within the layered metasediments and between the metasedimentary rocks and granitic intrusions (Figs. 2 and 3).

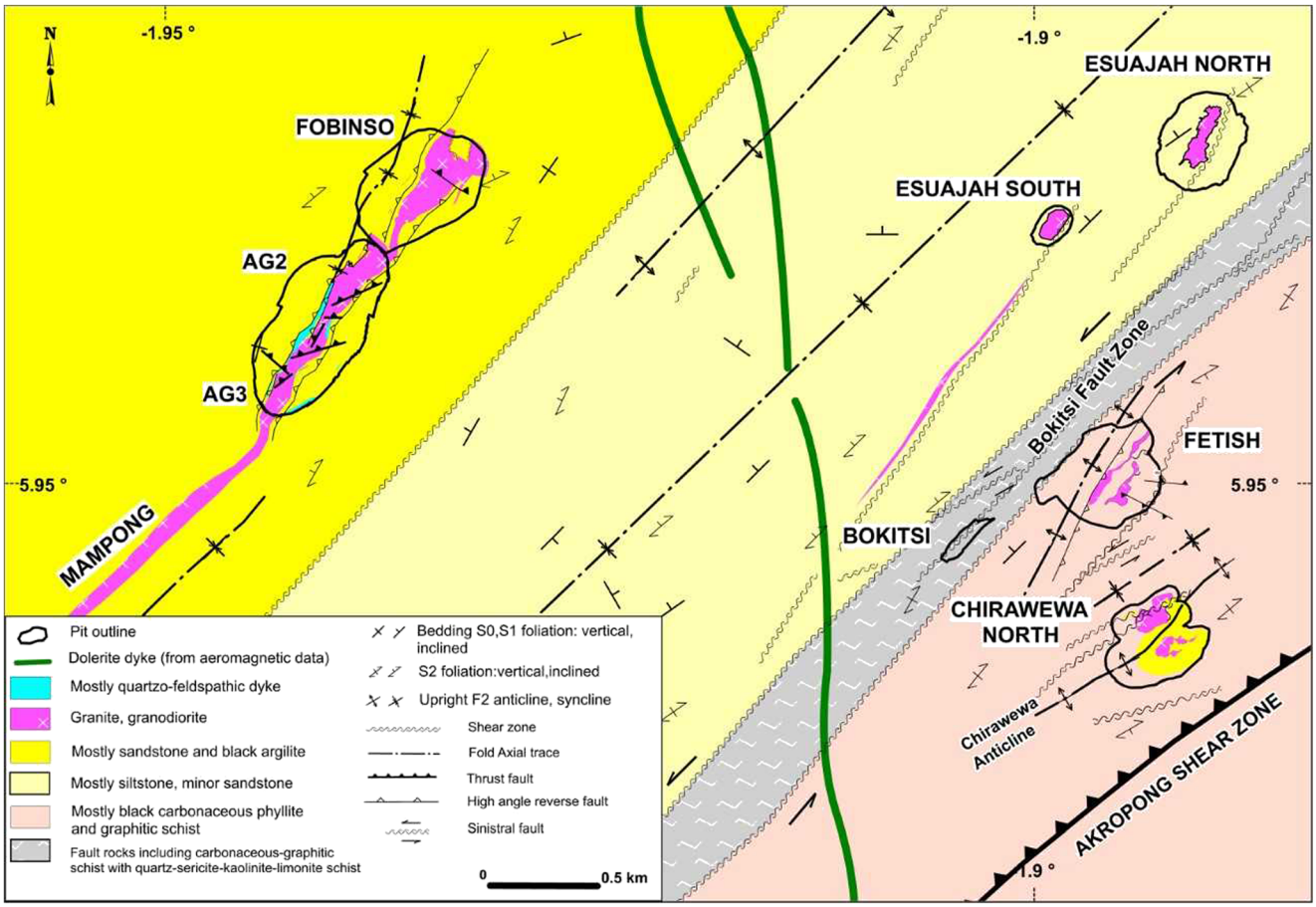

Fig. 2 Simplified geology and structural setting of the gold deposit cluster at the Edikan gold mine, Kumasi Basin, southwestern Ghana

On the basis of geological setting and mineralization style, the Paleoproterozoic (Birimian) gold deposits at Edikan can be subdivided into two groups:

- Mixed, granitoid- and fault zone-hosted gold deposits (e.g., Fetish, Bokitsi, and Chirawewa) to the east of the left lateral strike-slip Bokitsi fault zone (Fig. 2). Gold mineralization at these deposits is fault hosted where the host rocks are metasedimentary and vein hosted where the host is granitoid. Orebodies associated with this style of gold mineralization are characterized by a nuggetty grade distribution.
- The exclusively granitoid-hosted gold deposits to the west of the Bokitsi fault zone are exemplified by Esuajah North, Esuajah South, and AG2-AG3-Fobinso. The Esuajah North and South gold deposits are hosted in cylindrical granitoid plugs, whereas the AG2-AG3-Fobinso gold deposits, subject to this study, are contained in a single, continuous granodiorite dike. The granitoid-hosted gold deposits comprise disseminated sulfides and quartz-carbonate-gold veins. Gold distribution is relatively uniform throughout the host granitoid compared to the fault-hosted deposits.

The AG2-AG3-Fobinso gold deposits are hosted within a NE-SW-trending, ~70° NW-dipping granodiorite dike that extends for more than 4.7 km along strike and ranges in thickness from about 75 to 160 m (Figs. 2 and 3). Deep exploration drilling has followed the ore shoots (and host rock) to a vertical depth of over 450 m and with gold mineralization (and the host dike) remaining open at depth. The principal intrusive rock at AG2-AG3-Fobinso consists of an equigranular, white to light gray quartz-phyric granodiorite. At the mesoscopic scale, the granodiorite is massive and without trace of any penetrative foliation.

Local deformation

Detailed pit mapping indicates a complex polyphase deformation history at Edikan (Figs. 2 and 3; Table 1). Three distinct generations of structures have been identified in the open pits and in diamond drill holes. The timing of these structures is defined by the subscript "D_{Edk}," used hereafter to indicate the local structural events recognized in the Edikan gold camp.

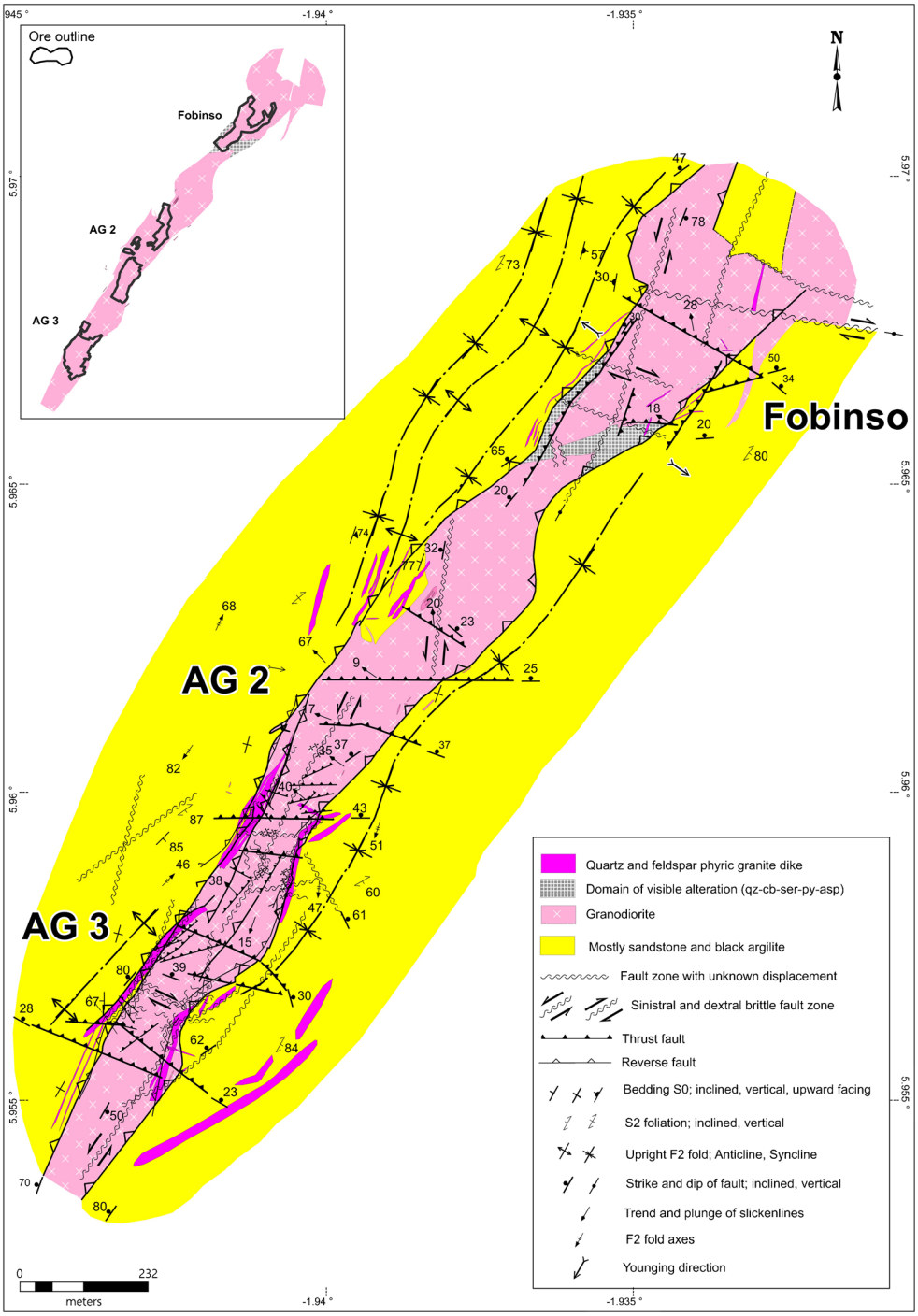

Fig. 3 Synoptic litho-structural map of the granitoid dike-hosted AG2-AG3-Fobinso gold deposits and surrounding metasedimentary country rocks

$D1_{Edk}$ event: The earliest structural fabric recognized at Edikan is manifested as a low-angle or bedding-parallel cleavage (S_1) and associated E-W-striking recumbent folds (F_1). This fabric appears to be preserved only locally within the hinges of younger F_2 folds. The significance of *$D1_{Edk}$* remains unresolved due to poor exposure and penetrative reworking of *$D1_{Edk}$* fabrics during later deformations.

$D2_{Edk}$ event: A second, penetrative fabric (S_2) and axial-planar to upright, tight to isoclinal, NE-SW-striking, gently to moderately NE- and SW-plunging F_2 folds is present everywhere in the Edikan camp (Figs. 2 and 3). The S_2 cleavage dips steeply either to NW or SE and clearly overprints both S_0 and S_1. Superposition of F_2 on F_1 folds has produced type-3-like interference patterns (Ramsay 1967). The doubly plunging nature of the F_2 folds suggests that they are either non-cylindrical and/or underwent post-D_{2Edk} modification. Crosscutting relationships indicate that the granitoid dike hosting the AG2-AG3-Fobinso gold deposits intruded an

anticlinal fold hinge (F_{2Edk}) in the metasedimentary country rocks as indicated by opposite younging directions recorded on either side of the dike (Fig. 3). Field evidence suggests that the dike was emplaced late during or post-D_{2Edk}, possibly during late or post-tectonic relaxation that created space/permeability and allowed melt ascent into the upper crust.

The contacts between the rheologically stronger granitoid dike and the weaker metasedimentary wall rocks are marked by faults that formed during D_{2Edk}. These structures, addressed here as D_{2Edk} boundary faults, are the dominant fault structures at AG2-AG3-Fobinso (Figs. 3 and 4a, b). The NE-SW-striking and, on average, 70° NW-dipping D_{2Edk} boundary faults are defined by about 2–15-m-wide structural corridors comprising abundant graphitic and clay-rich slip surfaces, discontinuous breccia bodies, and strongly foliated wall rock slivers. In addition, the structural corridors exhibit down-dip slickenlines marked by quartz and muscovite that, together with up-dip stepped fibers, indicate a top-to-the-SE reverse displacement along the D_{2Edk} boundary faults. In many places, the hanging walls of individual slip planes preserve evidence for rotation of S_0-S_1-S_2, indicating reverse displacement and implying a double-plunging geometry of the F_2 folds. However, the latter may be a result of D_{3Edk}.

$D3_{Edk}$ event: Most of the brittle deformation structures in the gold-bearing granitoids at Edikan can be linked to a single D_{3Edk} event. D_{3Edk} faults mapped and recorded within the open pits are mainly (a) low-angle contractional faults with pitches ≥ 60° (in their majority reverse faults with pitches ≥ 80°) that dip towards NW and N at ~ 30°, (b) left lateral oblique-slip contractional faults (with 30° < pitch < 60°) dipping towards N, and (c) strike-slip faults at different strikes, but mainly N-S, ENE-WSW, and NE-SW (Fig. 5). The low-angle contractional faults exhibiting either reverse or right lateral oblique-slip displacements crosscut the D_{2Edk} boundary faults, but they do not exhibit more than one generation of slickenlines plunging gently to moderately to the NW (Fig. 5a, b).

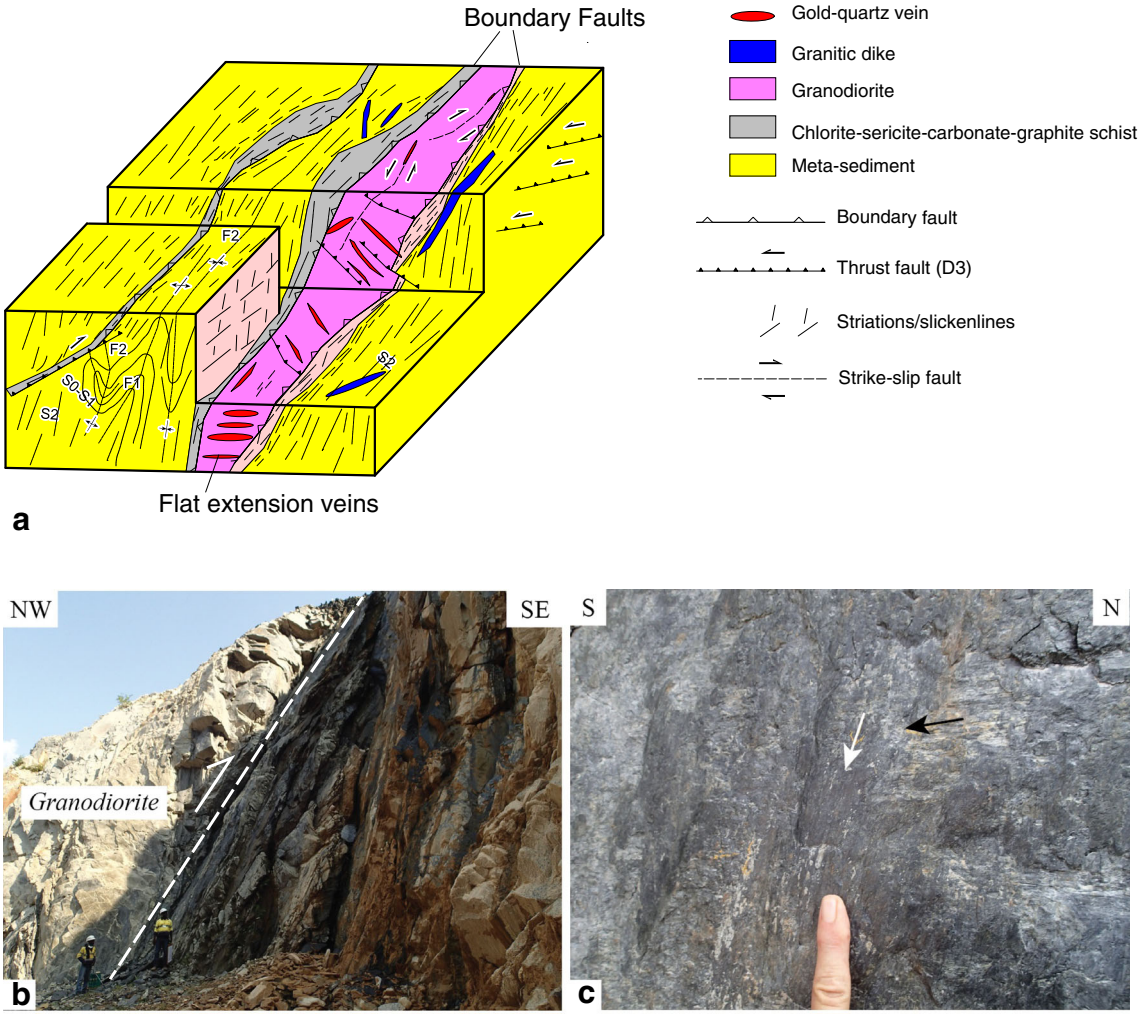

Fig. 4 (**a**) Schematic 3D model of structural and geological relationships at the AG2-AG3-Fobinso gold deposits. (**b**) Outcrop of a D_{2Edk} boundary fault, a major high-angle reverse fault (dip direction-dip angle: 315–70°), in the Fobinso pit wall. This fault is developed in and forms the structural footwall of the AG2-AG3-Fobinso gold deposits (view towards the north); (**c**) Down-dip slickenlines overprinted by subhorizontal slickenlines on a graphitic fault surface associated with the $D2_{Edk}$ boundary fault at Fobinso

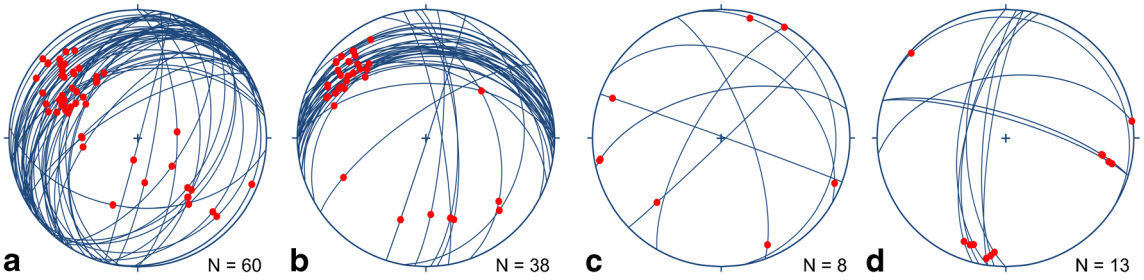

Fig. 5 Equal area, lower hemisphere projections showing the orientation of the early contractional and late extensional brittle faults at AG2-AG3-Fobinso. **a** Dip-slip contractional faults (pitch > 60°). **b** Oblique-slip contractional faults (30° < pitch > 60°). **c** Strike-slip contractional faults (pitch ≤ 30°). **d** Strike-slip extensional faults (pitch ≤ 30°). The dip-slip and oblique-slip low-angle contractional faults (**a**, **b**) are the principal mineralized structures in the deposits. The red dots represent measured slickenlines

On the other hand, two generations of slickenlines have been observed on the D_{2Edk} boundary faults (Fig. 4a, b). They correspond to reverse and left lateral oblique strike-slip displacements, respectively, with the latter slickenlines overprinting the former.

The different types (i.e., dip-slip, oblique-slip, strike-slip) of the faults point towards polyphase faulting related to compression and strike-slip tectonics. The $D3_{Edk}$ event is further examined in the next sections aimed at better constraining the paleostress history at the time of gold mineralization.

Syn-gold (D_{3Edk}) faults in granodiorite

The bulk of the gold-quartz vein mineralization at AG2-AG3-Fobinso is controlled by low-angle contractional faults that dip towards the NW at ~ 30° and the right lateral oblique-slip contractional faults dipping towards the N (Figs. 3, 5, and 6a, b). These faults range in thickness from less than 1 cm to more than 30 cm and have strike lengths ranging from about 15 m to more than 100 m (Fig. 6b). The thrusts and associated fault-fill veins contain well-developed slickenlines of quartz-calcite-sericite plunging consistently to the NW at ~ 30°, clearly indicating S- to SE-verging reverse displacement (Figs. 5 and 6c). Mineralized faults are in sharp contact with the undeformed granodiorite and fault boundaries usually coincide with discrete, very fine-grained phyllosilicate-quartz-calcite-rich slip planes. Within the faults, the granodioritic protolith has been transformed into a sericite-rich phyllonite with a weak foliation oriented parallel or at low angles to the slip planes. In rare occasions, this foliation exhibits a sigmoidal trajectory confirming the dominant reverse movement along flat-lying thrusts.

Additional mineralized structures include moderately to steeply dipping N-S- to NE-SW-striking faults that exhibit dip-slip (Fig. 5a) and oblique-slip contractional displacements (Fig. 5b).

The gold-quartz veins

Mineralized higher grade zones (> 1 g/t Au) in the granodiorite consist of gold-quartz veins and their altered wall rocks. All veins have similar mineralogy and alteration features. They are composed of white quartz, calcite, and white mica with subsidiary amounts of feldspar, pyrite, arsenopyrite, galena, chalcopyrite, sphalerite, tetrahedrite, and free gold in microfractures. Their alteration envelopes contain disseminated pyrite and arsenopyrite with visible gold grains often attached to the vein walls.

Following the classification of Sibson (1990, 1994), two main types of veins can be distinguished at Edikan: (1) fault-fill veins in both shallow and steeply dipping oblique-slip contractional faults and (2) extensional veins in flat hydraulic fractures developed between contractional faults (Figs. 7 and 8). Fault-fill veins are lenticular, variably deformed and brecciated, and generally bounded by faulted surfaces, clearly indicating that their development was accompanied by slip along the veins (Fig. 8a, b). They exhibit pinch-and-swell structures and incorporate tectonic slivers of altered wall rocks.

Flat extension veins comprise massive to vuggy vein quartz with little or no internal textural variation (Fig. 8c). Their relative direction of opening is indicated by the matching of irregularities along their foot- and hangingwalls as well as by the presence of steeply plunging quartz-calcite-muscovite-sericite fibers. The elongated fibers are usually perpendicular to the vein and the opening vector is subvertical at a high angle to the dip of the vein.

Paleostress analysis

A total of 119 fault planes with slickenlines were recorded during the geological mapping of the AG2-AG3-Fobinso pits. The large number of fault-slip data acquired as part of this study afforded us the opportunity to better define the stress regimes associated with D_{3Edk} and, thus, gold mineralization (Table 1). The observation in the field of faults exhibiting different generations of slickenlines (Fig. 4a, c) and movement senses points towards a complex deformation history during D_{3Edk}.

To define D_{3Edk} paleostress tensors, we used the software MyFault (MF) (http://www.pangaeasci.com) that uses several algorithms, including the widely accepted algorithm of

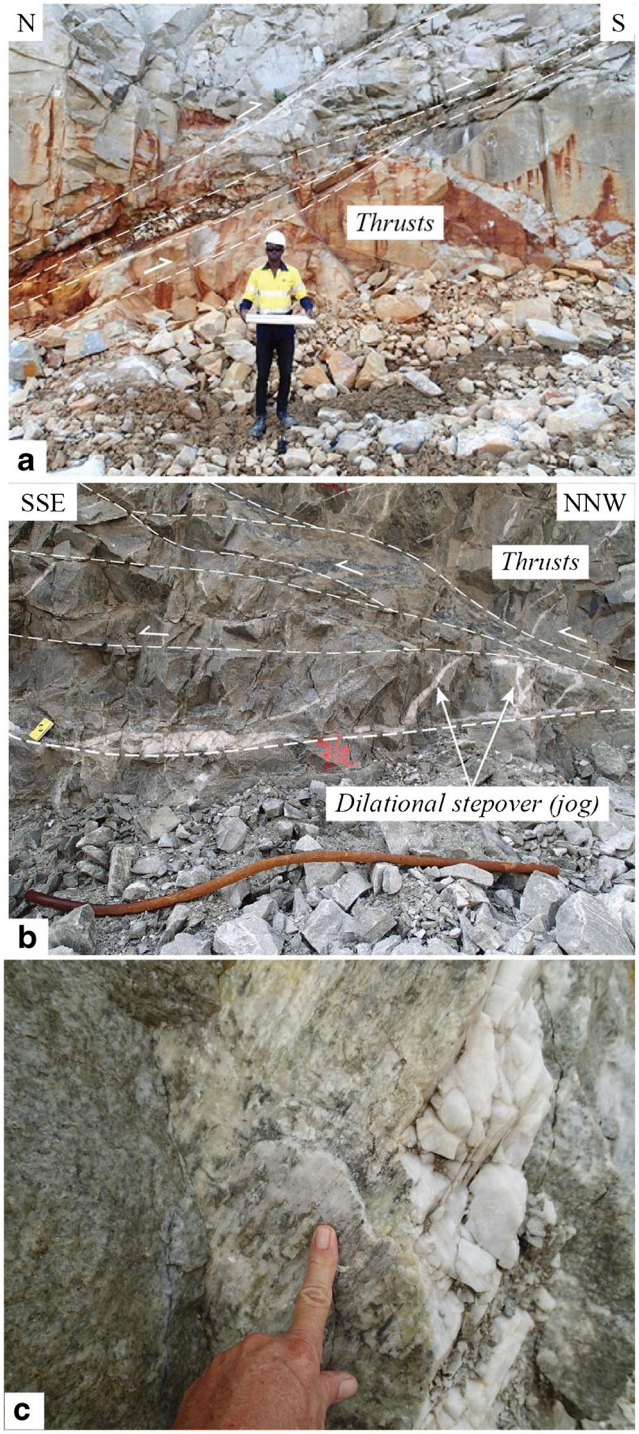

Fig. 6 Photographs illustrating the structural characteristics of D_{3Edk} low-angle thrust faults and associated gold-bearing quartz veins. **a** View towards the southeast of an E-W-striking thrust fault at AG2 dipping 30° N. A sample of the quartz vein and fault rock yielded an assay value of 7.4 g/t Au. **b** Anastomosing subhorizontal thrust faults and dilational stepover (Fobinso). **c** Hydrothermal slickenfibers of quartz and white mica on a slip surface developed along a fault-fill vein at Fobinso. The steps clearly indicate a reverse sense of movement along this low-angle contractional fault

Angelier (1984). For an accepted solution we used the threshold angle of 20° as the misfit angle (MA) minimization criterion; i.e., the angle between the real slickenline and the slip preference (SP) of the fault (SP is the expected theoretical fault-slip under a stress regime (Tranos 2012) and in stress inversion methods is considered to coincide with the maximum shear stress on the fault (Bott 1959)).

Stress inversion allows definition of the four parameters of the stress tensor: the orientations of the three principal stress axes (σ_1, σ_2, σ_3) and the stress ratio $R = (\sigma_2 - \sigma_3)/(\sigma_1 - \sigma_3)$ with $0 \le R \le 1$ (Etchecopar et al. 1981; Delvaux and Sperner 2003), which expresses the magnitude of σ_2 relative to the magnitudes of σ_1 and σ_3. The algorithm of Angelier (1984) minimizes the variations in the non-slip stress among the faults (i.e., the shear stress component in the fault plane normal to the slip direction), leading to an overdetermined set of linear equations. These equations are solved by the standard least squares techniques, giving the three principal stresses and their direction.

For the purpose of the stress regime characterization, we adopted the stress types of Tranos et al. (2008) that are based on the vertical position of the principal stress axes and the stress ratio. These stress types are for:

1. Compressional stress regimes: TRP: transpression (σ_2 or σ_3 vertical and $R \le 0.125$), TRP-PC: transpression to pure compression (σ_3 vertical and $0.125 < R < 0.375$), PC: pure compression (σ_3 vertical and $0.375 \le R \le 0.625$), PC-RC: pure to radial compression (σ_3 vertical and $0.625 < R < 0.875$), and RC: radial compression (σ_3 vertical and $0.875 \le R$); It is interesting to mention that TRP and TRP-PC describe a "hybrid" compression where both contractional dip-slip and strike-slip faults are optimal for activation, whereas PC, PC-RC, and RC describe the "real" compression under which only dip-slip and oblique-dip-slip contractional faults are optimal for activation (Tranos 2018).
2. Strike-slip regimes: TRP: transpression (σ_2 or σ_3 vertical and $R \le 0.125$), TRP-SS: transpression to pure strike-slip (σ_2 vertical and $0.125 < R < 0.375$), SS: pure strike-slip (σ_2 vertical and $0.375 \le R \le 0.625$), SS-TRN: pure strike-slip to transtension (σ_2 vertical and $0.625 < R < 0.875$), and TRN: transtension (σ_1 or σ_2 vertical and $0.875 \le R$).
3. Extensional stress regimes: RE: radial extension (σ_1 vertical and $R \le 0.125$), RE-PE: radial to pure extension (σ_1 vertical and $0.125 < R < 0.375$), PE: pure extension (σ_1 vertical and $0.375 \le R \le 0.625$), PE-TRN: pure extension to transtension (σ_1 vertical and $0.625 < R < 0.875$), and TRN: transtension (σ_1 or σ_2 vertical and $0.875 \le R$).

The terms transpression and transtension are used here as stress terms (i.e., as defined by Harland (1971) and Marrett and Peacock (1999)). As such, they are similar to the

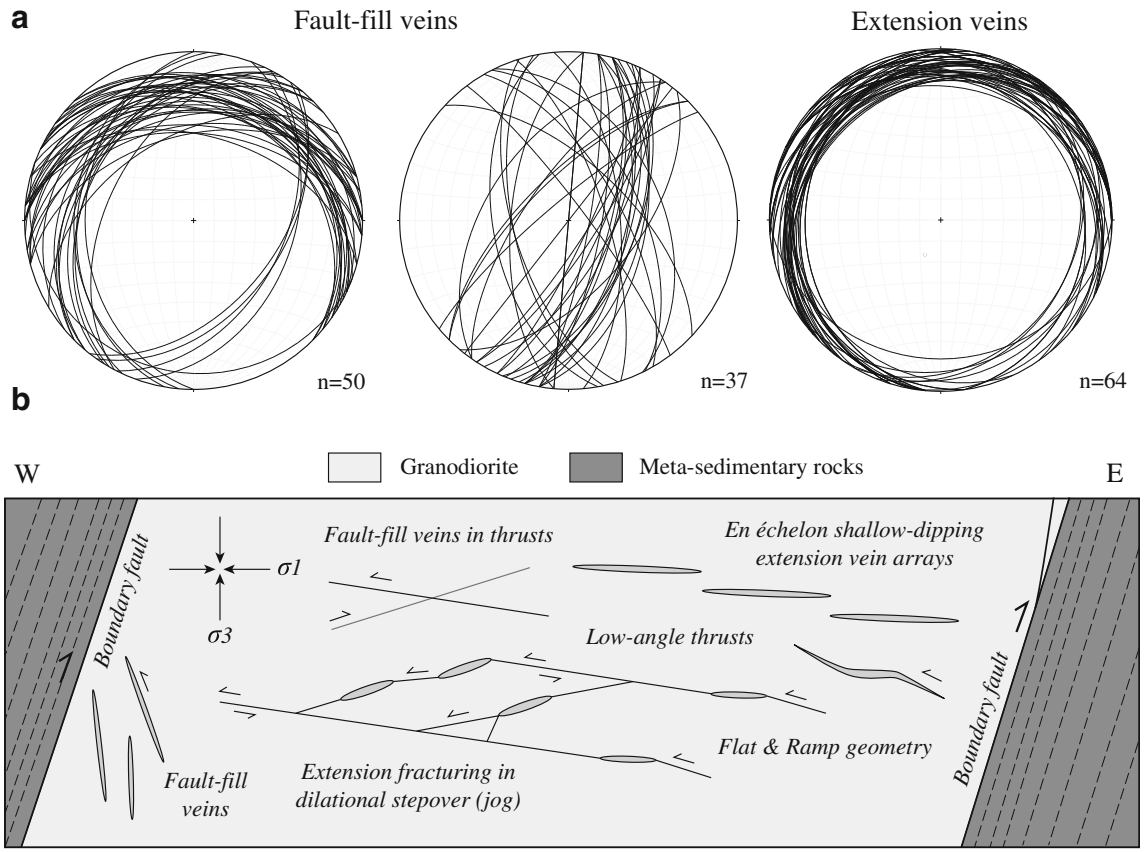

Fig. 7 **a** Equal area, lower hemisphere projections of gold-bearing veins at AG3-AG2-Fobinso. **b** Schematic sketch (not to scale) summarizing the geometry and pattern of the mineralized, granitoid-hosted fault-fracture mesh

definitions of axial compression ($\sigma_1 \geq \sigma_2 = \sigma_3$) and axial extension ($\sigma_1 = \sigma_2 \geq \sigma_3$) as proposed by Lisle (1979).

With MF, the 119 fault-slip data define a best-fit stress tensor, *T*, under which the mean misfit angle (MMA) of the fault-slip data is greater than 20° and 69 out of 119 fault-slip data have MA ≤ 20° (Table 2). The resolved stress tensor, T_{20}, with only the fault-slip data that have MA ≤ 20°, is almost similar to the previous one showing that this solution predominates due to the large number of fault-slip data that can be activated by it taking into account the MA. However, as recently shown by Tranos (2017, 2018) solutions with MMA > 20° and a large number of fault-slip data with MA > 20° might indicate that the input fault-slip data are heterogeneous and hard to distinguish them with the best-fit stress inversion methods.

Therefore, considering the initial fault-slip dataset heterogeneous, we applied the recently proposed separation and stress inversion method TRM (Tranos 2015). TRM is a semi-automatic graphical method that uses new additional constraining criteria about the geometric, kinematic, and dynamic compatibility of the faults driven by Andersonian stress regimes as they based on the slip preference analysis (SPA) (Tranos 2012, 2013, 2015). Based on these criteria, the TRM separates the heterogeneous fault-slip data into homogeneous groups including only the TR-compatible faults. The Andersonian state of stress is considered because any oblique-slip as evidenced by Bott (1959) can be generated on pre-existing faults with a vertical principal stress direction as in the Andersonian model (1905) and the shear stress orientation on a given plane depending solely on the principal stress orientation and the stress ratio, i.e., the Wallace-Bott hypothesis (Wallace 1951; Bott 1959). Consequently, there is no need for the principal stress directions to rotate away from Anderson's (1905) recommended positions. In TRM, the heterogeneous fault-slip data are separated into homogeneous groups by taking into account not only the MA as the best-fit stress inversion methods do (e.g., Carey and Brunier 1974; Angelier 1984, 1989) or the common orientation of the principal stress axes as previous methods do (e.g., the Right Dihedron method of Angelier and Mechler 1977) but also the stress ratio compatibility. The stress ratio compatibility is described by faults with such slickenlines that define a common stress ratio among them, i.e., the stress ratio of the driving stress tensor. In TRM the optimal resolved stress tensor is defined so that most of the TR-compatible faults to have MA ≤ 20° and the smallest MMA. However, in our application, the optimal stress tensors are more strictly defined not from all the TR-compatible faults, but only those having MA ≤ 20°, and secondly the smallest MMA.

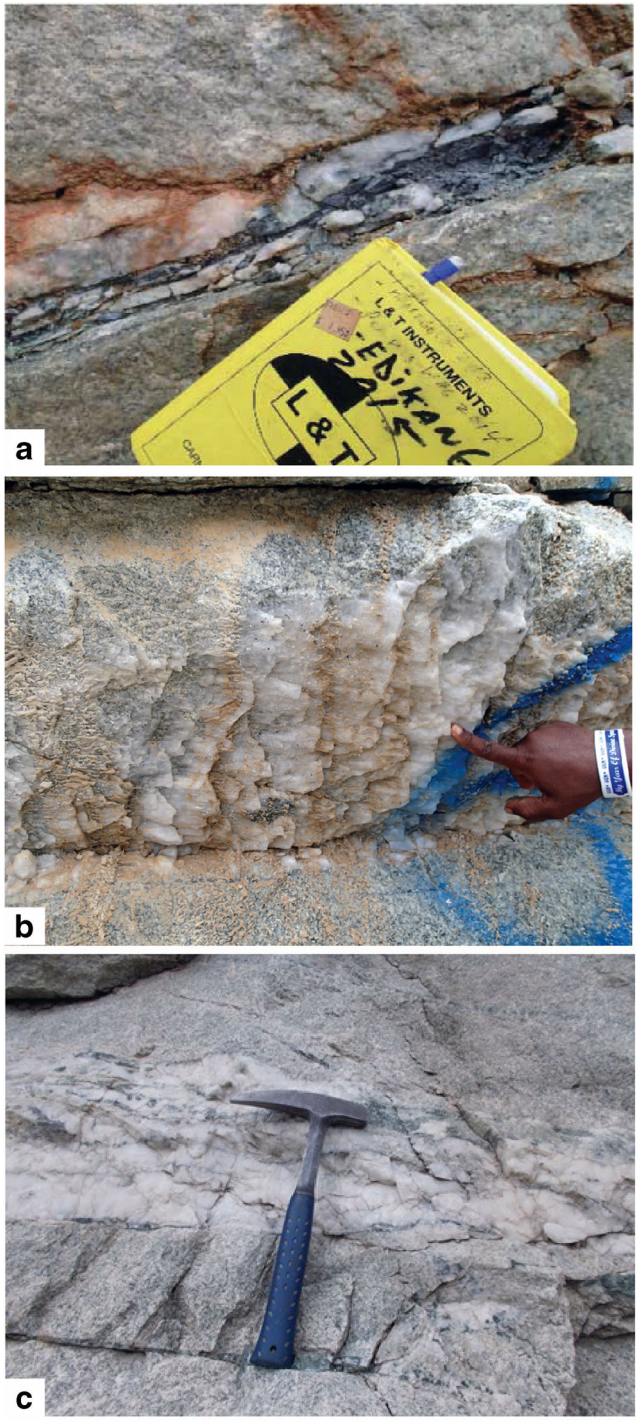

Fig. 8 **a** Fault-fill vein controlled by a gently N-dipping contractional fault. **b** Fault-fill vein with quartz slickenfibers developed along the slip plane of a NE-striking, left lateral strike-slip fault. **c** Shallow dipping extensional vein

In TRM, the trend of either the axes of infinitesimal shortening (P) or extension (T) (i.e., the kinematic P or T axes of Marrett and Allmendinger 1990) of the "optimal" faults is used as a first approximation for finding the σ_1 or σ_3 horizontal axis of the optimal stress tensor. In particular, for all compressional and extensional stress regimes, reverse and normal faults, respectively, are the most optimally oriented for frictional reactivation at close to Andersonian orientations (Healy et al. 2006; Tranos 2012, 2013), whereas strike-slip faults are also considered in the case of "hybrid" compressional stress regimes.

The application of the TRM indicates that the P axes of the optimal contractional faults in the dataset ($n = 106$), either these are dip-slip or strike-slip faults, define similar trends for the σ_1 horizontal axis. This implies the existence of two compressional stress regimes with similar σ_1 trend, which cannot be distinguished with the use of a best-fit stress inversion method (Tranos 2018). Because of this, the contractional fault-slip data that define the first optimal TRM stress tensor were excluded from the initial dataset, and afterwards, a second optimal TRM stress tensor is found. In particular, the application of the TRM defines the following optimal Andersonian stress tensors (Table 2):

1. T1 stress tensor (Fig. 9a, Table 2) with σ_1, σ_2, and σ_3 axes at 127°–00°, 037°–00°, and 127°–90°, respectively, and $R = 0.25$. This tensor explains 85 fault-slip data with MMA equal to 8.3° and constrains a pure compression-transpression (PC-TRP) stress regime. The activated faults are mainly (a) NW-dipping low- to medium angle thrusts and (b) N-dipping low- to medium-angle right lateral contractional faults;
2. T2 stress tensor (Fig. 9b, Table 2) with σ_1, σ_2, and σ_3 axes at 120°–00°, 120°–90°, and 030°–00°, respectively, and $R = 0.36$. This tensor explains only 6 fault-slip data with MMA equal to 5.2° and constrains a transpression-strike-slip (TRP-SS) stress regime. The activated faults are mainly (a) right lateral NE-SW- to ENE-WSW-striking medium to high-angle oblique and strike-slip faults dipping towards the NW to NNW and (b) left lateral NNW-SSE striking high-angle strike-slip faults;
3. T3 stress tensor (Fig. 9c, Table 2) with σ_1, σ_2, and σ_3 axes at 144°–00°, 144°–90°, and 054°–00°, respectively, and $R = 0.80$. This tensor explains only 12 extensional fault-slip data with MMA equal to 5.2° and constrains a strike-slip-transtension (SS-TRN) stress regime. The activated faults are mainly (a) N-S to NNE-SSW-striking left lateral strike-slip faults dipping towards the W-WNW and (b) right lateral high-angle strike-slip faults striking E-W.

T1, T2, and T3 stress tensors activate fault-slip data that have been found in the field to overprint each other. In particular, based on slickenline overprinting relationships along common fault planes and crosscutting relationships observed along faults, the T2 and T3 fault-slip data represent younger activations than the T1 fault-slip data. As a result, T1 to T3 fault-slip data should be considered as activations of the incremental stages of the D_{3Edk} event.

Table 2 The resolved stress tensors defined from the fault-slip data recorded in the three pits. Stress types according to Tranos et al. (2008)

ST		*n*	nt	FT_E	FT_C	TR (COMP)	σ_1	σ_2	σ_3	*R*	ST REG	MMA	FT (MA ≤ 20°)
T	MF	119	119				111°–06°	201°–06°	334°–81°	0.38	PC	25.6°	70
T_{20}	MF	70	69				116°–02°	207°–03°	356°–86°	0.3	PC-TRP	7.7°	69
T1	TRM	119			106	85	127°–00°	037°–00°	127°–90°	0.25	PC-TRP	8.3°	85
T2	TRM	119			21	6	120°–00°	120°–90°	030°–00°	0.36	TRP-SS	5.2°	6
T3	TRM	119		13		12	144°–00°	054°–90°	054°–00°	0.8	TRN	5.2°	12
T1	MF	85	79				126°–00°	036°–07°	217°–83°	0.33	PC-TRP	7.7°	79
T2	MF	6	6				310°–01°	044°–75°	220°–15°	0.72	SS-TRN	6.6°	6
T3	MF	12	12				154°–20°	310°–68°	061°–08°	0.8	SS-TRN	3.2°	12
T2-T3	MF	18	18				307°–31°	105°–57°	211°–10°	0.84	SS-TRN	19.1°	13

PC pure compression, *TRP* transpression, *TRN* transtension, *SS* strike-slip, *ST* stress tensor, *n* number of input fault-slip data, *nt* number of fault-slip data considered in the solution, FT_E extensional faults, FT_C contractional faults, *TR(COMB)* TR-compatible faults, *R* stress ratio, *ST REG* stress regime, *MMA* mean misfit angle, *FT(MA ≤ 20°)* number of fault-slip data with misfit angle (MA) ≤ 20°. T_{20} = the resolved stress tensor with fault-slip data having MA ≤ 20°

The fact that the T2 stress tensor was defined from a subset of the original dataset (i.e., by excluding the T1 fault-slip data) compelled us to investigate whether other fault-slip data from the initial dataset may be dynamically compatible with the T2 stress tensor by taking into account MA ≤ 20°. The application of the T2 stress tensor on the initial dataset shows that 39 out the 119 fault-slip data can be dynamically compatible with it. Apart from the strike-slip faults, T2 can also activate right lateral, oblique-slip, contractional faults dipping to the north. The similarity (or difference) between the T1 and T2 stress tensors can be easily checked by finding the Stress Tensor Discriminator Faults (STDF), i.e., the fault-slip data that can be activated by either tensor T1 or T2, but not from both of them as recently proposed by Tranos (2015). Taking into account the whole dataset of 119 fault-slip data, we defined that the STDFs for the T1-T2 data is 73.5%, for T1 is 69.4% and for T2 is only 33.3%, verifying that the T2 tensor cannot be distinguished in the initial fault-slip dataset with use of a best-fit stress inversion method.

The application of the MF to the fault-slip data from which the T1, T2, and T3 stress tensors were defined with the TRM calculates stress tensors that are shown in Table 2. The merged T2 and T3 fault-slip data, which both define strike-slip stress regimes, indicate that their activation cannot be facilitated by a single strike-slip stress tensor since the MMA is close to 20° and 5 fault-slip data, almost the number of the T2 fault-slip data, have MA > 20°. However, it is worth mentioning that the resolved T2 stress tensor is derived from a very small dataset (i.e., < 9 fault-slip data) and, thus, may not be robust since, according to Orife and Lisle (2003), such solutions might result from randomly generated fault-slip. More field data would be needed to better constrain the proposed T2 stress regime. On the other hand, to consider a single strike-slip tensor (T2-T3), instead of two is not the best option because many of the fault-slip data included in the T2 and T3 are incompatible even when applying the MA minimization criterion.

Dynamics of fault-fill and flat horizontal veins during T1, T2, and T3 stress regimes

As described above, the fault-fill and flat extensional veins formed in a dynamic tectonic environment during progressive D_{3Edk} deformation. It is therefore appropriate to test their dynamics in relation to the T1, T2, and T3 stress regimes. The results of this exercise allow for a better understanding of the relative importance of shearing versus dilation behaviors along faults that are being actively deformed (Ferrill and Morris 2003; Ferrill et al. 1998). This test uses a series of seven mean surfaces of different dip direction and dip angle that describe in general the different sets of the recorded fault-fill and flat extensional veins mapped in the open pits. These mean surfaces are tested for whether they can be activated under the T1, T2, and T3 stress regimes by defining their respective slip preference (SP), slip tendency (Ts), and dilation tendency (Td). Ts is the ratio of shear stress to normal stress on a surface (Morris et al. 1996), whereas Td is the ratio $(\sigma_1 - \sigma_n)/(\sigma_1 - \sigma_3)$ (Moeck et al. 2009), where σ_n is the resolved normal stress of the driving stress regime.

All calculations were undertaken according to Tranos (2015) and assuming dry conditions (i.e., fluid pore pressure was not taken into account). In addition, the following stress magnitudes were adopted as default values: (a) the magnitude of the greatest principal stress (σ_1) was considered equal to 100 MPa and (b) the cohesionless frictional sliding envelope was constructed for an internal friction angle of 45°, which means that the ratio σ_3/σ_1 equals 0.18, and thus the minimum principal stress (σ_3) takes the magnitude of 18 MPa. In this way, the maximum slip tendency value conveniently equals

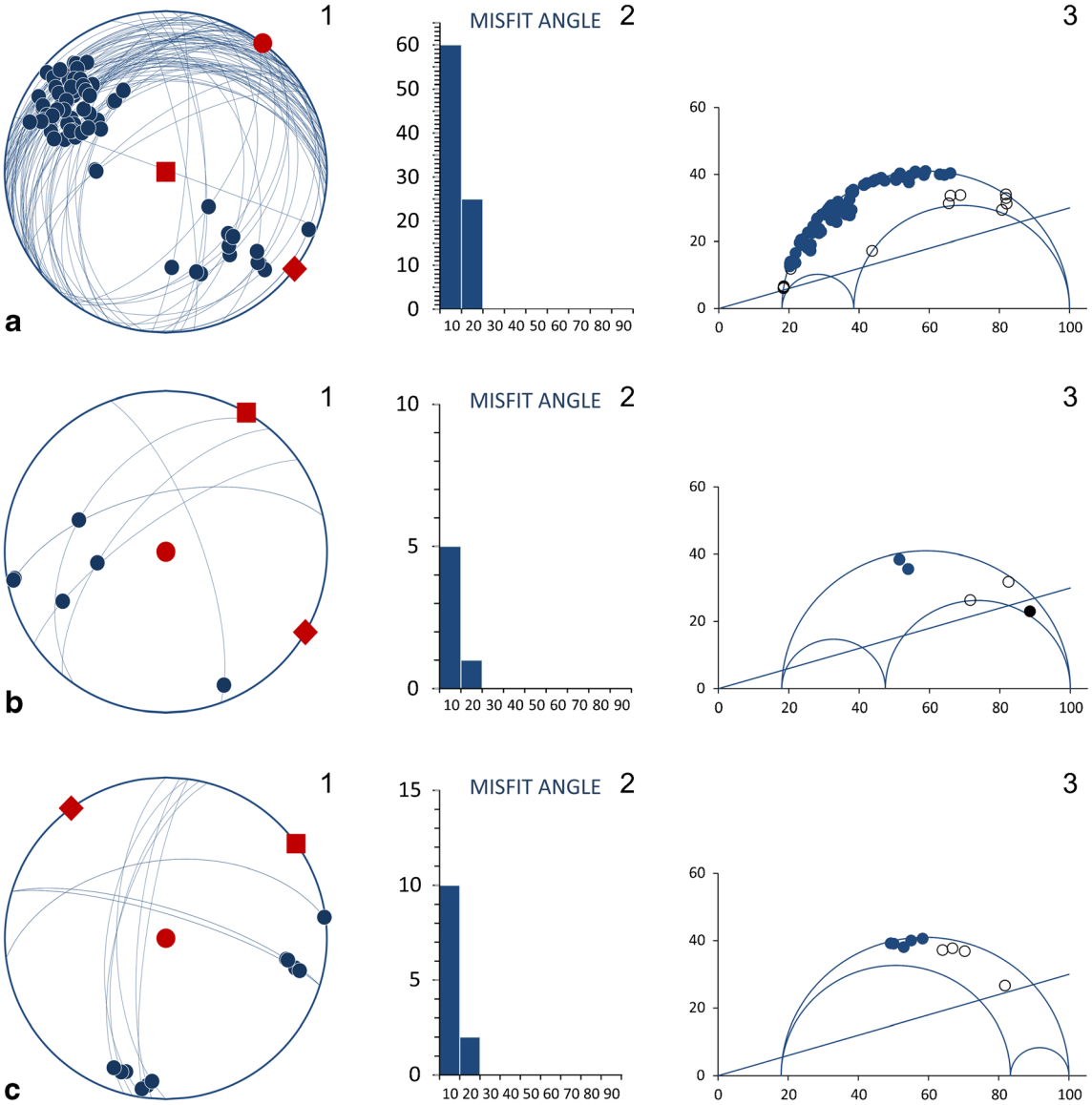

Fig. 9 The results of the application of the TRM (Tranos 2015) on the 119 fault-slip data recorded in AG2-AG3-Fobinso open pits. **a** T1, **b** T2, and **c** T3 are the optimal resolved stress tensors with misfit angle (MA) ≤ 20°. Explanation: 1. Equal area, lower hemisphere projection of the fault-slip data; 2. MA distribution of the fault-slip data; 3. Mohr diagram of the fault-slip data. Blue solid balls show the faults having slip tendency (Ts) (the ratio of shear stress to normal stress as introduced by Morris et al. (1996)) (Ts) ≥ 0.6. Open balls show the fault-slip data with Ts < 0.6. The black balls show fault-slip data below the blue line which is the lowest initial friction curve at the frictional angle $\varphi = 16.7°$

one. The magnitude of σ_2 is fixed by the stress ratio R as a function of the magnitudes σ_1 and σ_3.

This slip and dilation tendency analysis is a technique that permits rapid and easy visual assessment of stress states and related potential fault activity. Therefore, under the different stress regimes we found the following:

1. T1: pure compression-transpression

This stress regime, based on the Ts (as shown in Table 3), mainly facilitates the occurence of V1 and V2 fault-fill veins that are the principal gold-bearing veins found in the low-angle contractional faults dipping to the N and NW and to a minor extent, the occurence of the V6 fault-fill veins along faults that might form oblique segments to the low-angle contractional faults (Fig. 10a). All of these fault-fill veins might form a swarm along faults that are characterized by slip compatibility and therefore can be considered as being contemporaneous.

In addition, the flat extension veins, V7, which are tabular gold-bearing veins dipping at an average angle of 18° to the NW (Table 3; Fig. 8c), indicate high Ts and Td under the T1 stress regime as would be expected from oblique-extension veins (Lafrance 2004). Oblique-extension veins crystallize in transitional tensile fractures, which open and propagate while subject to a shear traction (Blenkinsop 2008). They are inclined with respect to the σ_1 axis by less than 26° thus fitting well with

Table 3 The relation of gold-bearing fault-fill and extension veins under the T1 stress regime

Au veins	DIPD	DIPA	SP	SOS	Ts	Td
V1	307	34	90	IX	0.87	0.69
V2	12	30	49	ID	0.70	0.90
V3	110	68	121	IS	0.37	0.20
V4	66	64	150	IS	0.59	0.66
V5	311	71	81	ID	0.28	0.11
V6	257	60	143	IS	0.63	0.58
V7	300	18	96	IS	0.93	0.91

SP slip preference, *SOS* sense of slip, *Ts* slip tendency, *Td* dilation tendency, *IX* reverse, *ID* right lateral reverse, *IS* left lateral reverse

Table 4 The relation of the gold-bearing fault-fill and extension veins under the T2 stress regime

Au veins	DIPD	DIPA	SP	SOS	Ts	Td
V1	307	34	77	ID	0.38	0.44
V2	12	30	142	ND	0.36	0.71
V3	110	68	127	IS	0.24	0.12
V4	66	64	1	NS	0.75	0.65
V5	311	71	46	ID	0.23	0.10
V6	257	60	170	IS	0.62	0.51
V7	300	18	90	IX	0.29	0.58

SP slip preference, *SOS* sense of slip, *Ts* slip tendency, *Td* dilation tendency, *IX* reverse, *ID* right lateral reverse, *IS* left lateral reverse

Healy's theory (i.e., the theory of faulting by microcrack linkage; Healy et al. 2006), and their walls have slipped as those of reverse faults as shown by SP in Table 3.

2. T2: transpression-strike-slip

In the T2 stress regime, the maximum and minimum principal stress axes are in a horizontal position (Fig. 10b). As shown in Table 4, under T2 stress regime, only V4 and V6 veins obtain values of $Ts \geq 0.6$. The V4 and V6 veins are antithetic, having formed along NNW-SSE-striking, steeply dipping, left lateral strike-slip faults. On the other hand, the gently N-dipping V2 veins attain Ts values < 0.6, but Td values > 0.6 illustrating that their tendency for dilation dominates their mode of formation.

3. T3: strike-slip-transtension

In this regime, the veins that have high Ts and Td and are compatible with the T3 stress regime are V4 and V6 (Fig. 10c, Table 5). However, these veins, instead of aligning parallel to the faults activated by the T3 stress regime, strike oblique to the N-S- to NNE-SSW-striking and W- to WNW-dipping left lateral strike-slip faults and the right lateral high-angle strike-slip faults striking E-W. Moreover, their formation is facilitated if the host planes are characterized by left lateral oblique-slip kinematics.

On the other hand, V3 and V5 vein sets attain significantly low Ts and Td values for all T1 to T3 stress regimes as shown in Tables 3, 4, and 5. Hence, formation of these veins may have been related to local fluid pressure increases along pre-existing fault planes. Alternatively, they may have been emplaced along discontinuities developed as mode I fractures formed by extension (e.g., Pollard and Aydin 1988).

Deposit-scale gold distribution

The Surpac® mining software was used to produce a three-dimensional rendering of the combined grade control and exploration drilling gold assay data aimed at facilitating better visualization and evaluation of ore trends at the AG2-AG3-Fobinso gold deposits.

Figure 11a, which represents a slice through the three-dimensional model along a horizontal plane 100 m below

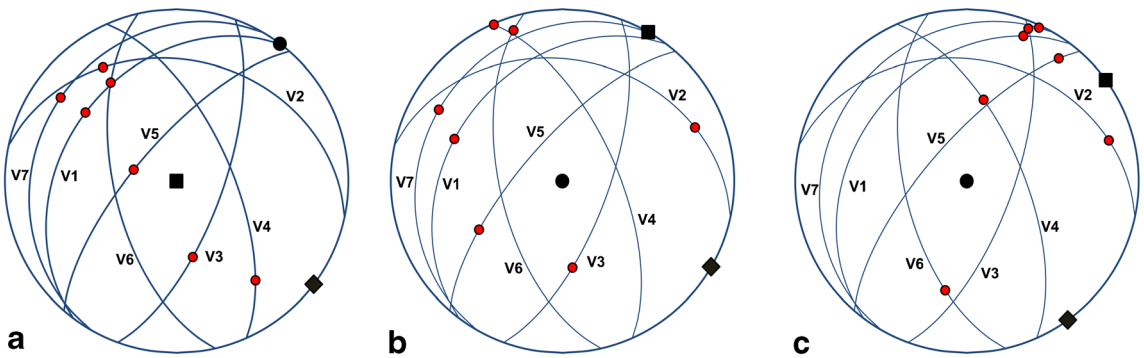

Fig. 10 Lower hemisphere equal area projections of the fractures (fault-fill veins (V1–V6) and flat extensional veins (V7)) under the **a** T1, **b** T2, and **c** T3 stress regimes. Explanation: Red balls show the slip preference, i.e., the theoretical slip vector of the fractures under the stress regimes, solid rhomb, circle, and square shows the position of σ_1, σ_2, and σ_3 principal stress axes

Table 5 The relation of gold-bearing fault-fill and extension veins under the T3 stress regime

Au veins	DIPD	DIPA	SP	SOS	Ts	Td
V1	307	34	161	IS	0.16	0.16
V2	12	30	148	ND	0.31	0.29
V3	110	68	5	NS	0.47	0.30
V4	66	64	58	NS	0.86	0.81
V5	311	71	167	IS	0.18	0.07
V6	257	60	42	NS	0.78	0.69
V7	300	18	175	IS	0.11	0.20

SP slip preference, *SOS* sense of slip, *Ts* slip tendency, *Td* dilation tendency, *IX* reverse, *ID* right lateral reverse, *IS* left lateral reverse

surface, serves to illustrate the spatial distribution of the < 0.5, 0.5–1.0, and > 1.0 g/t Au grade shells and superimposed interpreted mineralized fault arrays. Based on the relationships shown in Fig. 11a, the spatial distribution of the highest gold values (i.e., > 1.0 g/t Au grade shells) appears to be controlled by ~ NE-SW-striking faults, and crosscutting ENE-WSW- to NW-SE-striking thrust faults. The model also illustrates well that the highest gold values are localized where the granodiorite dike is thinner than average. Such "dike necks" are conspicuously associated with complex 3D vein and fault networks and pervasive hydrothermal alteration. In plan view, high-grade ore lenses strike NNE-SSW to NW-SE, acutely oblique to the D_{2Edk} boundary faults. At Fobinso, two high-grade lenses occur in close proximity to a right-hand bend in the intrusive contact. A similar situation is identified at AG2 where the main high-grade pod coincides with a discrete right-hand bend along the intrusive contact. At AG3, the main high-grade pod is also located close to a discrete right-hand bend (Fig. 11a).

As evident in a vertical long section oriented parallel to the NE-SW-striking granodiorite dike (Fig. 11b), high-grade ore shoots plunge at 30–40° to the NE and developed at the intersection of flat-lying veins and thrusts with steeply dipping structures (Fig. 11c).

Discussion

Deformation history and relative timing of gold deposition

The local deformation history recorded at Edikan is compared hereafter to the prolonged structural and magmatic evolution of the Kumasi Basin and Ashanti granite-greenstone belt in southwest Ghana (Table 1).

D_{1Edk}, the first deformation event recorded at Edikan, was a ductile deformation event that produced rarely preserved recumbent folds with ~ E-W-oriented axial planes and an early bedding-parallel foliation (chlorite-muscovite laths), S_{1Edk}. This early greenschist facies event has also been recognized at the giant Obuasi gold mine (D_{1Ob} in Allibone et al. 2002; Feybesse et al. 2006; Fougerouse et al. 2017). D_{1Edk} deformation is interpreted to have been linked to N-S-directed shortening. However, the kinematics of this early deformation could not be constrained for Edikan due to its poor preservation and strong overprinting and modification by later events.

The subsequent D_{2Edk} deformation event can be correlated to similar deformation events (D_2) recognized across southwest Ghana. These events resulted in the formation of a pervasive NE-SW-trending regional foliation (S_2) dominating the tectonic grain (e.g., Feybesse et al. 2006; Perrouty et al. 2012; Salvi et al. 2016). D_2 occurred under greenschist facies conditions as indicated by the presence of chlorite-muscovite and albite in the schist zones.

Progressive deformation under NW-SE compression (D_{2Edk}) began with the formation of NE-SW-trending F_{2Edk} folds and associated axial-planar cleavage (S_{2Edk}). Ongoing compression eventually resulted in fold lock-up, formation of high-angle reverse faults, and, ultimately, development of a regionally extensive fold-thrust belt. Basin-type granitoids at Edikan intruded late during this phase of deformation although some intrusive contacts, for example those of the granodiorite dike at AG2-AG3-Fobinso, became sites of high-angle reverse faulting (i.e., D_{2Edk} boundary faults).

The last significant deformation event at Edikan was the brittle D_{3Edk} event, having generated a network of brittle faults with contrasting kinematics. D_{3Edk} can be subdivided into three stress regimes, T1, T2, and T3, each characterized by specific fault kinematics. T1 was defined by a transpression-pure compression (TRP-PC) (i.e., "hybrid compression") stress regime with a WNW-ESE-oriented axis of contraction, whereas the subsequent T2 and T3 were defined by strike-slip regimes. More precisely, T2 was a TRP-SS stress regime with a contraction axis trending WNW-ESE, while T3 was a SS-TRN regime with a contraction axis trending NW-SE. Based on our field observations (e.g., gently plunging slickenlines crosscutting steeply plunging slickenlines), the strike-slip regimes are younger than the "hybrid" compression. Therefore, the D_{3Edk} deformation event is best described as a progressive event that switched from an early "hybrid" compression to subsequent strike-slip tectonics with the respective contraction axes having slightly changed in orientation from WNW-ESE to NW-SE.

From an economic geology point of view, similar transient events that recorded changes from dominantly transpression to transtension tectonics have been documented in the > 8.5 Moz Siguiri gold district of Guinea and interpreted as a result of the reduction of the deviatoric stress tensor, in turn requiring a major reduction of the differential stress (Lebrun et al. 2017). Similarly, stress switches have been documented

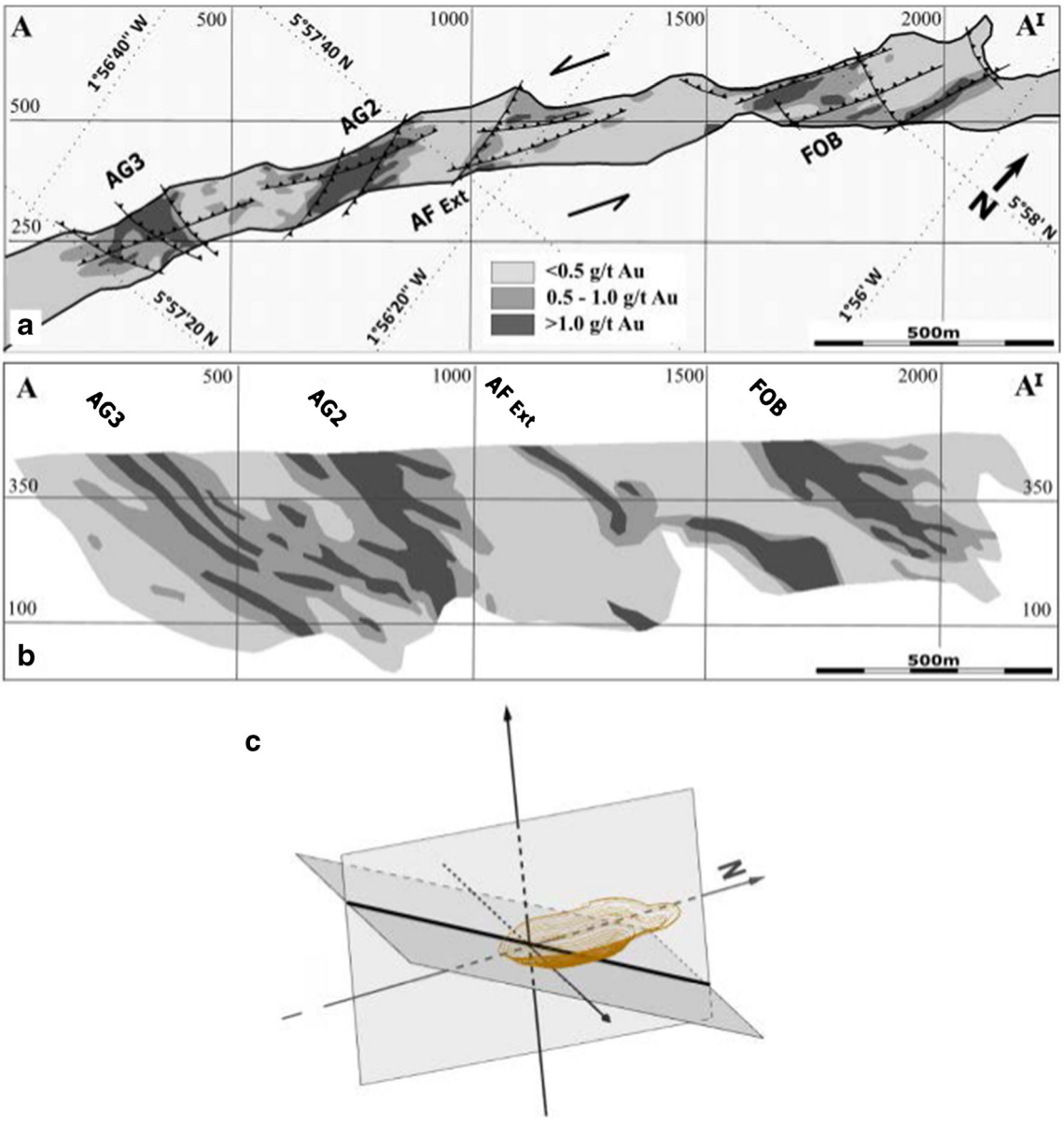

Fig. 11 **a** Trace of the mineralized granodiorite on the 360 m (~ 100 m below surface) reduced level and also illustrating isograds of gold content. The general trend of the high-grade mineralization is controlled by the presence of two sets of brittle faults. **b** NE-SW-oriented long section (A-A^{I}) illustrating the dominant NE plunge of the ore shoots. **c** Schematic diagram showing the crosscutting relationships between the steep veins and the gently N-dipping veins with the final pit shell of AG2 and AG3 deposits. The intersection line between the steep NE-SW-striking veins and about E-W-striking, gently dipping structures plunges NE parallel to the ore shoot

at the Ashanti mine at Obuasi (Allibone et al. 2002) and for several additional West African gold deposits including the Morilla (> 7 Moz), Loulu (> 3.5 Moz), and Sadiola Hill (> 8 Moz) mines in Mali (see McFarlane et al. 2011; Lawrence et al. 2013; Masurel et al. 2017). These authors consider stress switches as critical processes for lowering of the deviatoric and differential stresses (e.g., Lebrun et al. 2017) and, consequently, promoting fluid flow and concomitant gold mineralization. It is, therefore, suggested that the recorded stress switches at Edikan, combined with fault reactivation, provided important mechanisms leading to deposit-scale focusing of ore-bearing fluids and gold deposition in fault-fracture meshes that developed in and were superimposed on competent granitoid dikes. Data from field mapping suggest that gold mineralization was essentially a single protracted D_{3Edk} event related to successive shifts in the local tectonic regimes.

Considering the bigger picture, it is worthwhile noting that gold mineralization at the nearby Pampe (Fig. 1) is thought to have formed under similar conditions of far field shortening (D_{3Pam} of Salvi et al. 2016). Another example similar to Edikan is Damang (Fig. 1) where part of the gold deposit is hosted by subhorizontal quartz vein arrays and low-angle

thrusts that formed during a period of WNW-ESE-directed shortening (D_{3Tkw} of Tunks et al. 2004). The relative timing of gold mineralization at Edikan is therefore best correlated with the transpressional sinistral-reverse reactivation of the NE-SW-striking and NW-dipping Konongo-Ashanti-Prestea fault that juxtaposed the Kumasi Basin against the Ashanti Belt (D_{4Ob} of Allibone et al. 2002; Feybesse et al. 2006).

Interpretation of the mineralized fault-vein system

The gold-bearing brittle faults and gold-bearing quartz veins hosted by the granodiorite dike at AG2-AG3-Fobinso display a diverse range of orientations and slip directions, implying strong structural controls on their mode of emplacement and kinematics. They developed under incremental changes in the overall protracted D_{3Edk} stress regimes T1, T2, and T3. Ubiquitous low-angle reverse and oblique-slip faults and gently dipping oblique-extension veins are consistent with formation during the early T1 stress regime while the variably oriented high-angle faults fit best with the subsequent T2 and T3 stress regimes.

The gold-bearing, granitoid-hosted T1 structures form an interconnected system of gently to moderately dipping fractures typical of fault-fracture meshes as typically developed in compressional-transpressional tectonic regimes ($\sigma_v = \sigma_3$; Sibson 2017). The prerequisite for development and growth of such meshes is fluid pressures approaching or exceeding lithostatic levels (Sibson et al. 1988). Such conditions are in good agreement with the fault-valve mechanism invoked for many gold-bearing orogenic vein systems developed in compressional-transpressional tectonic regimes (Boullier and Robert 1992; Cox 1999, 2005; Robert et al. 1995; Sibson 1996, 2017).

An additional, interesting aspect to be considered here is the evidence of reverse to reverse-oblique and strike-slip faulting along the steeply dipping D_{2Edk} boundary faults as well as the rarely mineralized steeply dipping D_{3Edk} faults cutting the granodiorite. The strikes and dips of these discontinuities are at high angle (> 60°) to σ_1. Such steeply dipping, misoriented faults are fundamental for fracture meshes and hydraulic extension fractures to be generated (Sibson and Scott 1998). According to Sibson (1985), steep faults in horizontal compressional stress regimes are misoriented precluding effortless slip and those observed at Edikan were not expected to be activated during D_{3edk} hybrid compression (T1 stress regime). Reactivation of misoriented faults is only possible under conditions of high fluid pressure (Sibson et al. 1988). The presence of flat oblique-extension veins and their internal open-space filling textures provide good evidence of high fluid pressures during mineralization. This implies that steep faults with a wide range of orientations were reactivated with variable kinematics depending of their strike and dip. The reactivation increments exclude the faults that were subparallel to σ_1-σ_3, σ_2-σ_3, or σ_1-σ_2 planes.

In summary, geological and structural relations indicate that the mineralized fault-fracture mesh at AG2-AG3-Fobinso formed late in the tectonic history of the Edikan district and a complex polyphase deformation history involving a switch from an early "hybrid" compression (T1) to a later dominantly strike-slip stress regimes T2 and T3. The brittle deformation style combined with the style of mineralization is directly related to the massive nature of the host granodiorite dike and competency contrast between the intrusive body and surrounding metasedimentary country rocks.

Ore shoot location and geometry

Overall, sinistral-reverse shear along the D_{2Edk} boundary faults at AG2-AG3-Fobinso, as well as the imbricated thrust array, are interpreted to indicate that gold mineralization within the granitoid dike was localized by decameter-scale contractional jogs that were active during D_{3Edk}. Similarly, the orientation and reverse shear sense of the steeply E-dipping gold-bearing structures points towards contractional structures whose formation is kinematically compatible with a sinistral transpressive event. These NE-SW-striking structures are interpreted to have developed in contractional damage zones generated by strain accommodation around the restraining jogs.

The correlation between higher grade gold mineralization and right-hand flexures and intrusive "necks" (Fig. 11a) indicates that restraining bends were sites of high damage intensity and fluid flux (e.g., Cox et al. 2001). Geometrically, the 30–40° NE-plunging high-grade ore shoots in Fig. 11b are consistent with the intersection of shallow dipping extension vein arrays and low-angle thrusts with steeper NNE-SSW- to NE-SW-striking fault zones (Fig. 11c). Similar gold-bearing low-angle and steep contractional structures have been recognized in the Archean St-Ives gold district in Western Australia (Nguyen et al. 1998; Cox and Running 2004; Miller et al. 2010).

Field observations are consistent with the fault-fracture mesh centered upon the rigid granodiorite dike at AG2-AG3-Fobinso having provided a favorable environment for gold deposition. It is very likely that the competency contrast between the granodiorite dike and less competent metasedimentary wall rocks gave rise to strain incompatibility and rock rotation linked to shearing, increased fracturing, permeability, and focusing of gold-bearing fluids into the fault-fracture mesh that formed within the competent dike (Weinberg et al. 2004).

Similar controls on ore shoot location and geometry have been reported for several orogenic gold deposits worldwide, including the Archean Peron, Ferderber, and Dumont gold mines in the Archean Abitibi greenstone belt of eastern Canada (Robert 1990; Belkabir et al. 1993; Robert and Poulsen 2001).

Conclusions

Based on detailed mapping and observations made at the AG2-AG3-Fobinso open pits (Kumasi Basin, southwest Ghana) as well as our interpretation and analysis of the structural data, we can draw the following conclusions:

1. The structural data presented herein are consistent with a classic orogenic model for the granitoid-hosted gold deposits at Edikan.
2. The studied AG2-AG3-Fobinso gold deposits were emplaced late during the Eburnean orogeny and exhibit typical features of syntectonic mesothermal deposits including (i) structural association with polyphase faulting related with an early "hybrid" compression to late strike-slip tectonics, (ii) fault-fill and extensional/oblique-extensional gold-quartz veins forming part of a larger fault-fracture mesh that formed in a dominantly compressional tectonic regime, and (iii) quartz-carbonate-gold veins with low sulfide contents and associated carbonate-quartz-sericite-pyrite-arsenopyrite wall rock alteration assemblage.
3. The fault-slip data can be subdivided into three groups defining the dominant stress regimes that governed the protracted D_{3Edk} deformation stage. The recorded gold-quartz veins were grouped into seven sets of fault-fill fractures that were related to T1, T2, and T3 stress regimes of the D_{3Edk} deformation event. The early stage of D_{3Edk} coincided with T1 ESE-WNW-oriented horizontal shortening that activated low-angle dip- and oblique-slip contractional faults and facilitated the emplacement of the principal gold-bearing fault-fill veins (V1-V2) and oblique-extensional veins (V7). Gold-quartz veins emplaced and activated during the later T2 and T3 strike-slip stress regimes are restricted to steeply dipping fault-fill veins. These veins are of little importance economically because they represent only a minor volume of the gold ore contained within the studied deposits.
4. Stress switches described in this study are not unique to the granite-hosted deposits at Edikan and similar processes are widely recognized at other gold deposit locations across the West African Craton and commonly constrained to the period 2080 to 2070 Ma (Lebrun et al. 2017).
5. Structural timing relationships between mineralized structures and the similar mineralogical association and alteration features of all types of veins/fault zones are compatible with a single protracted gold mineralizing event during T1, T2, and T3 stress regimes of D_{3Edk}. The various types of auriferous veins recorded at AG2-AG3-Fobinso can be reasonably considered as being penecontemporaneous.
6. Our study demonstrates that the irregular shape of the granitoid dike at AG2-AG3-Fobinso influenced the spatial distribution of the gold-bearing structures. Pods of higher grade gold mineralization are clearly spatially associated with the shortened segments of right-hand bends along the dike and consistent with contractional jogs containing abundant shallow and steeply dipping veins and faults. The NE plunge of the high-grade domains (i.e., ore shoots) observed in long section is controlled by the intersections of shallow dipping and steep structures. Interestingly, the plunge of the ore shoots is suborthogonal to the tectonic transport direction as indicated by slickenlines recorded on thrust fault surfaces. This geometric relationship indicates that the gold-bearing quartz vein-filled fault-fracture meshes define ore shoots that are synchronous with the development of their host faults (cf. Robert and Poulsen 2001).
7. The geologic and structural observations presented here are largely derived from structural mapping and would benefit from more advanced analytical studies designed to unravel the nature of the mineralizing fluids, the distribution and styles of alteration, the geochemical signature of the ore, and the age of the mineralization. An estimation of the time gap between dike emplacement and gold mineralization would be of particular interest.

Acknowledgements The authors wish to thank all the staff from the mine geology and exploration departments at Edikan for their fruitful insight and discussions during the field work. The work presented here was initiated when the first author was employed with SEMS Exploration and benefited from discussion with former colleagues Simon Meadows Smith and John Coates. Doug Jones, Kevin Thompson, Eric Dontoh, Francis Azumah, Albert Mortey, Kwabena Asante, Sarfo Kantanka, and Gary Brabham are thanked for their insights and constructive discussions on the geology of Edikan. The authors also gratefully acknowledge Perseus Mining Ghana Ltd. for the assistance with field work logistics. Perseus Mining Ltd. is thanked for the permission to publish this work. We wish to gratefully acknowledge AMIRA International and its industry sponsors for their support of the WAXI-2 Project (P934A). L. Baratoux, O. Vanderhaeghe, and an anonymous reviewer are gratefully appreciated for their insightful and critical reviews that helped to improve the manuscript. We would also like to thank B. Lehmann and H. Frimmel for their excellent editorial assistance.

References

Adadey K, Clarke B, Théveniaut H, Urien P, Delor C, Roig JY, Feybesse JL (2009) Geological map explanation—map sheet 0503 B (1: 100000), CGS/BRGM/Geoman, Geological Survey Department of Ghana (GSD). No MSSP/2005/GSD/5a

Allibone A, McCuaig TC, Harris D, Etheridge M, Munroe S, Byrne D (2002) Structural controls on gold mineralization at the Ashanti gold deposit, Obuasi, Ghana. Soc Econ Geol Spec Publ 9:65–93

Allibone A, Heyden P, Cameron G, Duku F (2004) Paleoproterozoic gold deposits hosted by albite- and carbonate-altered tonalite in the Chirano District, Ghana, West Africa. Econ Geol 99:479–497

Anderson EM (1905) The dynamics of faulting. Transact Edinburgh Geol Soc 8:387–402

Angelier J (1984) Tectonic analysis of fault slip data sets. J Geophys Res 89(B7):5835–5848

Angelier J (1989) From orientation to magnitudes in paleostress determinations using fault slip data. J Struct Geol 11:37–50

Angelier J, Mechler P (1977) Sur une méthode graphique de recherche des contraintes principales également utilisable en tectonique et en séismologie : la méthode des dièdres droits. Bull Soc Géol France 7: 1309–1318

Baah-Danso E (2011) The structural evolution of the Subika deposit, Ahafo, Sefwi Belt, Ghana. Univ Western Australia, MSc Thesis

Baratoux L, Soderlund U, Ernst RE, de Roever E, Jessell MW, Kamo S, Naba S, Perrouty S, Metelka V, Yatte D, Grenholm M, Diallo DP, Ndiaye PM, Dioh E, Cournède C, Benoit M, Baratoux D, Youbi N, Rousse S, Bendaoud A (in press) New U-Pb baddeleyite ages of mafic dyke swarms of the West African and Amazonian Cratons: implication for their configuration in supercontinents through time, *in* Srivastava RK, Ernst RE, Peng P. (eds) (2019) Dyke swarms of the world—a modern perspective. Springer

Belkabir A, Robert F, Vu L, Hubert C (1993) The influence of dikes on auriferous shear zone development within granitoid intrusions: the Bourlamaque pluton, Val-d'Or district, Abitibi greenstone belt. Can J Earth Sci 30:1924–1933

Blenkinsop TG (2008) Relationships between faults, extension fractures and veins, and stress. J Struct Geol 30:622–632

Blenkinsop TG, Schmidt Mumm A, Kumi R, Sangmor S (1994) Structural geology of the Ashanti gold mine, Obuasi, Ghana. Geol Jahrb D 100:131–153

Bott MHP (1959) The mechanics of oblique slip faulting. Geol Mag 96: 109–117

Boullier AM, Robert F (1992) Paleoseismic events recorded in Archean gold-quartz vein networks, Val d'Or, Abitibi, Quebec, Canada. J Struct Geol 14:161–179

Carey E, Brunier B (1974) Analyse théorique et numérique d'un modèle mécanique élémentaire appliquè à l'étude d'une population de failles. C R Acad Sci <Paris> D 279: 891–894

Chudasama B, Porwal A, Kreuzer OP, Brutera K (2016) Geology, geodynamics and orogenic gold prospectivity modelling of the Paleoproterozoic Kumasi Basin, Ghana, West Africa. Ore Geol Rev 78:692–711

Cox SF (1999) Deformational controls on the dynamics of fluid flow in mesothermal gold systems. In: McCaffrey K, Lonergan L, Wilkinson J (eds) Fractures, fluid flow, and mineralization, Geol Soc London Spec Publ, vol 155, pp 123–140

Cox SF (2005) Coupling between deformation, fluid pressures, and fluid flow in ore-producing hydrothermal systems at depth in the crust. Econ Geol 100th Anniv Vol: 39–75

Cox SF, Running K (2004) The St Ives mesothermal gold system, Western Australia-a case of golden aftershocks? J Struct Geol 26: 1109–1125

Cox SF, Knackstedt MA, Braun J (2001) Principles of structural controls on permeability and fluid flow in hydrothermal systems. Soc Econ Geol, Rev Econ Geol 14:1–24

Delvaux D, Sperner B (2003) Stress tensor inversion from fault kinematic indicators and focal mechanism data: the TENSOR program. In: Nieuwland D (ed) New insights into structural interpretation and modelling, Geol Soc London Spec Publ, vol 212, pp 75–100

Duodu AJ, Loh GK, Baomah KO, Baba M, Hirdes W, Toloczyki M, Davis DW (2009) Geological map of Ghana1:1 000 000. Geological Department of Ghana (GSD)

Etchecopar A, Vasseur G, Daignieres M (1981) An inverse problem in microtectonics for the determination of stress tensors from fault striation analysis. J Struct Geol 3:51–65

Ferrill DA, Morris AP (2003) Dilational normal faults. J Struct Geol 25: 183–196

Ferrill DA, Morris AP, Jones SM, Stamatakos JA (1998) Extensional layer parallel shear and normal faulting. J Struct Geol 20:355–362

Feybesse JL, Billa M, Guerrot C, Duguey E, Lescuyer JL, Milési JP, Bouchot V (2006) The Paleoproterozoic Ghanaian province: geodynamic model and ore controls, including regional stress modeling. Precambrian Res 149:149–196

Fougerouse D, Micklewaite S, Ulrich S, Miller J, Godel B, Adams DT, McCuaig TC (2017) Evidence for two stages of mineralization in West Africa's largest gold deposit: Obuasi, Ghana. Econ Geol 112:3–22

Gelber BDJ (2018) A mineral systems approach to the development of structural targeting criteria for orogenic gold deposits in the Asankrangwa gold belt of the Kumasi Basin, South-west Ghana. Unpubl MSc Thesis, Rhodes University, Grahamstown, South Africa, 144 p

Harland WB (1971) Tectonic transpression in Caledonian Spitsbergen. Geol Mag 108:27–42

Healy D, Jones RR, Holdsworth RE (2006) Three-dimensional brittle shear fracturing by tensile crack interaction. Nature 439:64–67

Jessell M, Santoul J, Baratoux L, Youbi N, Ernst RE, Metelka V, Miller J, Perrouty S (2015) An updated map of West African mafic dikes. Afr J Earth Sci 112:440–450

Jessell MW, Begg GC, Miller MS (2016) The geophysical signatures of the West African craton. Precambrian Res 274:3–24

Lafrance B (2004) Conjugate oblique-extension veins in shear and tensile fracture systems at the Komis gold mine and Mufferaw gold prospect, northern Saskatchewan. Explor Mining Geol 13:1–9

Lawrence DM, Treloar PJ, Rankin AH, Harbidge P, Holliday J (2013) The geology and mineralogy of the Loulo mining district, Mali, West Africa: evidence for two distinct styles of orogenic gold mineralization. Econ Geol 108:199–227

Lebrun E, Miler J, Thébaud N, Ulrich S, McCuaig TC (2017) Structural controls on an orogenic gold system: the world-class Siguiri gold district, Siguiri Basin, Guinea, West Africa. Econ Geol 112:73–98

Lisle R (1979) The representation and calculation of the deviatoric component of the geological stress tensor. J Struct Geol 1:317–321

Marrett R, Allmendinger RW (1990) Kinematic analysis of fault-slip data. J Struct Geol 12:973–986

Marrett R, Peacock DCP (1999) Strain and stress. J Struct Geol 21:1057–1063

Masurel Q, Thébaud N, Miller J, Ulrich S, Hein KAA, Cameron G, Béziat D, Bruguier O (2017) Sadiola Hill: a world-class gold deposit in Mali. West Africa: Econ Geol 112:23–47

McFarlane CRM, Mavrogenes J, Lentz D, King K, Allibone A, Holcombe R (2011) Geology and intrusion-related affinity of the Morila Gold mine, southeast Mali. Econ Geol 106:727–750

Miller J, Blewett RS, Tunjic J, Connors K (2010) The role of early formed structures on the development of the world class St Ives Goldfield, Yilgarn, WA. Precambrian Res 183:292–315

Moeck I, Kwiatek G, Zimmermann G (2009) Slip tendency analysis, fault reactivation potential and induced seismicity in a deep geothermal reservoir. J Struct Geol 31:1174–1182

Morris AP, Ferrill DA, Henderson DB (1996) Slip tendency and fault reactivation. Geology 24:275–278

Nguyen PT, Cox SF, Harris HB, Powell CM (1998) Fault-valve behaviour in optimally oriented shear zones: an example at the Revenge gold mine, Kambalda, Western Australia. J Struct Geol 20:1625–1640

Oberthür T, Vetter U, Davis DW, Amanor JA (1998) Age constraints on gold mineralization and Paleoproterozoic crustal evolution in the Ashanti belt of southern Ghana. Precambrian Res 89:129–143

Orife T, Lisle RJ (2003) Numerical processing of paleostress results. J Struct Geol 25:949–957

Parra-Avila L, Bourassa Y, Miller J, Perrouty S, Fiorentini M, McCuaig TC (2015) Age constraints of the Wassa and Benso mesothermal gold deposits, Ashanti belt, Ghana, West Africa. J African Earth Sci 112:524–535

Perrouty S, Aillères L, Jesselll MW, Baratoux L, Bourassa Y, Crawford B (2012) Revised Eburnean geodynamic evolution of the gold-rich southern Ashanti belt, Ghana, with new field and geophysical evidence of pre-Tarkwaian deformation. Precambrian Res 204-205:12–39

Pigeois JP, Groves DI, Fletcher RI, McNaughton NJ, Snee LW (2003) Age constraints on Tarkwaian palaeoplacer and lode-gold formation in the Tarkwa-Damang district, SW Ghana. Mineral Deposita 38: 695–714

Pollard DD, Aydin A (1988) Progress in understanding jointing in the last century. Geol Soc Am Bull 100:1181–1204

Ramsay JG (1967) Folding and fracturing of rocks. McGraw-Hill Book Company, Inc., New York

Robert F (1990) Structural setting and control of gold-quartz veins the Val d'Or area, southeastern Abitibi Subprovince, *in* Ho SE, Robert F, Groves DI (eds) Gold and base metal mineralization in the Abitibi Subprovince, Canada, with emphasis on the Quebec segment. University of Western Australia, Geology Key Centre and University Extension, Publ 24: 164–209

Robert F, Poulsen KH (2001) Vein formation and deformation in greenstone gold deposits. Soc Econ Geol, Rev Econ Geol 14:111–155

Robert F, Boullier AM, Firdaous K (1995) Gold-quartz veins in metamorphic terranes and their bearing on the role of fluids in faulting. J Geophys Res 100(B7):12,861–12,879

Salvi S, Velásquez G, Miller JM, Béziat D, Siebenaller L, Bourassa Y (2016) The Pampe gold deposit (Ghana): constraints on sulfide evolution during gold mineralization. Ore Geol Rev 78:673–686

Sibson RH (1985) A note on fault reactivation. J Struct Geol 7:751–754

Sibson RH (1990) Faulting and fluid flow. *in* Nesbitt BE (ed) Fluids in tectonically active regimes of the continental crust. Mineral Ass Can, Short Course Handbook 18: 93–112

Sibson RH (1994) Crustal stress, faulting and fluid flow. Geol Soc Spec Publ 78:69–84

Sibson RH (1996) Structural permeability of fluid-driven fault-fracture meshes. J Struct Geol 18:1031–1042

Sibson RH (2017) Tensile overpressure compartments on low-angle thrust faults. Earth Planets Space 113:1–15

Sibson RH, Scott J (1998) Stress/fault controls on the containment and release of overpressured fluids: examples from gold-quartz vein systems in Juneau, Alaska; Victoria, Australia and Otago, New Zealand. Ore Geol Rev 13:293–306

Sibson RH, Robert F, Poulsen KH (1988) High-angle reverse faults, fluid-pressure cycling and mesothermal gold-quartz deposits. Geology 16:1666–1703

Tranos MD (2012) Slip preference on pre-existing faults: a guide tool for the separation of heterogeneous fault-slip data in extensional stress regimes. Tectonophysics 544-545:60–74

Tranos MD (2013) The TR method: the use of slip preference to separate heterogeneous fault-slip data in compressional stress regimes. The surface rupture of the 1999 Chi-Chi Taiwan earthquake as a case study. Tectonophysics 608:622–641

Tranos MD (2015) TR method (TRM): a separation and stress inversion method for heterogeneous fault-slip data driven by Andersonian extensional and compressional stress regimes. J Struct Geol 79: 57–74

Tranos MD (2017) The use of stress tensor discriminator faults in separating heterogeneous fault-slip data with best-fit stress inversion methods. J Struct Geol 102:168–178

Tranos MD (2018) The use of stress tensor discriminator faults in separating heterogeneous fault-slip data with best-fit stress inversion methods. II. Compressional stress regimes. J Struct Geol 107:153–162

Tranos MD, Kachev VN, Mountrakis DM (2008) Transtensional origin of the NE–SW Simitli basin along the Strouma (Strymon) Lineament, SW Bulgaria. J Geol Soc Lond 165:499–510

Tunks AJ, Selley D, Rogers JR, Brabham G (2004) Vein mineralization at the Damang Gold Mine, Ghana: controls on the mineralization. J Struct Geol 26:1257–1273

Wallace R (1951) Geometry of shearing stress and relation to faulting. J Geol 59:118–130

Weinberg RF, Hodkiewicz PF, Groves DI (2004) What controls gold distribution in Archean terranes? Geology 32:545–548

Yao Y, Robb LJ (2000) Gold mineralization in Paleoproterozoic granitoids at Obuasi, Ashanti region, Ghana: ore geology, geochemistry and fluid characteristics. South Afr J Geol 103:255–278